Characterization and Improvement of the Thermal Stability of TES Bolometers

Thesis by
Rita Frances Sonka

In Partial Fulfillment of the Requirements for the
Degree of
Bachelor of Science

CALIFORNIA INSTITUTE OF TECHNOLOGY
Pasadena, California

2018
(Defended May 22, 2018)

Rita Frances Sonka
ORCID: 0000-0002-1187-9781

ACKNOWLEDGEMENTS

In addition to my parents and personal friends, who have more generally supported me in my career, I would like to acknowledge a few wonderful people who have particularly supported my academic growth that led to this thesis.

I would like to thank Dr. Jamie Bock and Dr. Bryan Steinbach, my thesis advisers and mentors for two separate Summer Undergraduate Research Fellowship (SURF) projects, for their continued support throughout my time at Caltech. Thank you for that 2014 seminar that blew my mind and sparked the interest in inflation and the Cosmic Microwave Background that has led my scientific pursuits ever since. Thank you for the many weekly meetings, patient guidance, and general introduction to the world of academia.

I would like to thank the Caltech SURF office and the Caltech Senior thesis program as well for providing me such an incredible opportunity to pursue my research interests as an undergraduate.

I would like to thank several Bock lab members who encouraged me, lent me figures, and/or helped teach me the details of experimental work in physics and general and the Bock Lab in particular. Thank you to Cheng Zhang, Ahmed Mohamed, Howard Hui, Jonathen Hunacek, and Sinan Kefeli.

I would like to thank Anthony Turner, Krikor G. Megerian, and the Jet Propulsion Laboratory in general for their assistance in fabricating the detectors investigated in this thesis.

ABSTRACT

The successful detection and characterization of the B-modes in the Cosmic Microwave Background (CMB) would dramatically illuminate the physics of the inflationary era. The Observational Cosmology Group is iterating on bolometers in an attempt to detect this signal. The previous detector design became unstable in parts of its transition when adjusted for 220/270 GHz frequencies, limiting its use.

We study the mechanism of instability in these transition edge sensor (TES) bolometers used for ground based observations of the Cosmic Microwave Background (CMB) at 270GHz. The instability limits the range of useful operating resistances of the TES down to $\approx$ 50% of R_n, and due to variations in detector properties and optical loading within a column of multiplexed detectors, limits the effective on sky yield to $\approx$ 67 %.

Through comparison of 7 new detector thermal capacity designs and measurements of the electrical impedance of the detectors, we show the instability is due to the increased bolometer leg G for higher-frequency detection inducing decoupling of the palladium-gold heat capacity from the thermistor. We demonstrate experimentally that the limiting thermal resistance is due to the small cross sectional area of the silicon nitride bolometer island, and so is easily fixed by layering palladium-gold over an oxide protected TES. The resulting detectors can be biased down to a resistance $\approx$10% of R_n, improving the effective on-sky yield to $\approx$ 93 %.

We also investigate a possibly related, unexpected slope in the Aluminum calibration TES transition and determine that it is not due to phase separation, even accounting for the science TES thermal instability.

TABLE OF CONTENTS

Acknowledgements . . . iii
Abstract . . . iv
Table of Contents . . . v
List of Illustrations . . . vi
List of Tables . . . xi
Chapter I: Motivation and Introduction . . . 1
Chapter II: Background, Issue and Theory . . . 2
2.1 Transition Edge Sensor Bolometers . . . 2
2.2 The IV and PR curve of the Ideal TES . . . 3
2.3 Thermal instability issue . . . 6
2.4 Bolometer decoupling model . . . 8
2.5 Modification Logic and Designs . . . 10
2.6 The Aluminum PR curve investigation . . . 12
Chapter III: Methods: Data Acquisition . . . 15
3.1 IV curves data acquisition . . . 15
3.2 Superfast data acquisition . . . 19
3.3 Bolometer impedance acquisition . . . 19
Chapter IV: Methods: Analysis . . . 21
4.1 Titanium TES . . . 21
4.2 Aluminum TES . . . 23
4.3 Superfast . . . 24
4.4 Impedance . . . 24
Chapter V: Results . . . 26
5.1 Titanium IV curves . . . 26
5.2 Aluminum PR Slope Models and Fit Results . . . 27
5.3 Superfast preliminary results . . . 31
5.4 Impedance . . . 32
Chapter VI: Conclusions . . . 35
Bibliography . . . 36
Appendix A: Titanium sample IV, PR and transition-select plots for all types . . . 38
A.1 Characteristic IV plots . . . 38
A.2 PR transition-select plots . . . 41
A.3 Transition range graphs . . . 45

LIST OF ILLUSTRATIONS

Number *Page*

1.1 This plot of "signal strength/CMB signal strength" as a function of frequency shows the latest noise constraints on the B-mode signal, accompanied by the latest bounds on the signal's magnitude. The red patch shows allowed false-signal magnitudes of synchrotron radiation. The purple band shows allowed false-signal magnitudes from dust. The horizontal black lines are upperbounds on the B-mode signal's magnitude. Note how they have lowered enough that there is essentially no avoiding both the dust and synchrotron radiation errors, and one must be subtracted out regardless of what frequency the signal is pursued at. As the dust model is better constrained, it was chosen to use for subtraction. The 220/270 GHz range has negligible synchrotron radiation noise while still being somewhat close to the primary data taking range around 150 GHz, and thus is ideal for imaging the dust. Image Credit [4] 1

2.1 Basics of bolometers. Image credit: D.F. Santavicca, licensed under Creative Commons Attribution 3.0 2

2.2 Superconductor Temperature vs. Resistance. 2

2.3 The ideal IV and PR curves, as illustrated by one of our detectors after the instability issue was fixed. 3

2.4 Ideal TES thermal and electrical circuit. In the ideal case, the island and the TES are much better connected than the link through the island's legs to the bath, and thus they are at the same temperature, and the island's is the only relevant heat capacity because it dwarfs the TES's. 3

2.5 Results of derivation of Ideal TES, and also a comparison of ideal case to post-thesis modification reality. Compare to the bath temperature = 254mK run of the F type detector given in Fig. 2.7 (this specific run is reproduced here below this caption for easy comparison); this run had a $P_{thC} \approx 16$ pW which you can see from the PR curve in the right graph in this figure. $R_{shunt} \approx 3$ mΩ for our detectors. Compare this ideal PR curve to the actual PR curve for this run, the rightmost IV curve in the left graph of Fig. 2.7 (reproduced below). The general 1/x shape is correct for the in-transition region, as are the approximate magnitudes at each endpoint of the in-transition region. 5
2.6 Original (type A) detector characteristic IV and PR plots. 6
2.7 Fully functional (type F) detector IV and PR plot. 7
2.8 Bolometer thermal (black) and electrical (green) circuit. 8
2.9 Original SF data that helped prompt this thesis. 8
2.10 Above: Annotated photograph under microscope of a control group (A-type) detector. Below: Diagram of side view along blue line on the photograph, not to scale. In green: location of the relevant 150 μm^2 island cross section. Note the green dimensions line on the photograph had to be moved to the side; the side view green dimension line shows the relevant location along the island's length. 9
2.11 Photographs of the 8 bolometer designs. 12
2.12 The cuts of the aluminum transitions for the type D (above) and type F (below) detectors. Red lines mark the start and ends of the selected transition region from the data (blue). Note the differences in how the transitions end. 12
2.13 The early cutoff in the plot is due to a limitation of the equipment's ability to put large currents through the device. However, the large slope in the transition region was unexpected. 13
3.1 FPU # 1 temperature during the successful data-taking run is in pink. Note that the temperature of the detectors exceeds the FPU # 1 plane during the application of the critical current ("zapping") that occurred at the top of each peak, and for some time thereafter as data was taken. 16
3.2 An example of raw data for some of the IV curves at 254mK. Displays I-TES vs. I-bias, each in DAC [Data Acquisition and Control units]. 17

3.3 Simplified version of the TES circuit. The inductor is used to read out the circuit by projecting a magnetic field; ideally, there is only a negligible voltage drop across it when data is being read. 18
3.4 Type G "double transition" Rn failure IV plot. 19
4.1 Ideal superconductor resistance curve. Note that as per the heat equation, the power dissipated in the detectors is related to the temperature of the detectors; the more power dissipated, the higher a temperature difference will be established between the detectors and bath. 21
4.2 A particularly bad column (mce column 3) of Algorithm 1 (local standard deviation change) PR plot results for the 254 mK run. Consider, for example, the row 9 detector. Blank plots has failed or absent detectors, or failed SQUIDS. 22
4.3 The same column algorithm 1 failed on, much improved in the final algorithm. 22
4.4 These residuals are small compared to the actual values. 24
5.1 Type A transition range graph at a bath temperature of 254mK. The x axes are the current applied to the TES shunt resistors. The vertical line shows the optimal current where the largest number of detectors are operating simultaneously. In the left plot, horizontal bars show the limits of the in transition for each detector of type A. The right plot shows the count of in transition detectors for each bias current. . 27
5.2 Type F transition range graph at a bath temperature of 254mK. Compared to Fig. A.17, the stable bias regions are much wider for each detector. 27
5.3 Mean length in which a detector was usable (in R_{TES}/R_n %) vs. Temperature (in mK). Higher is better. Types A, B, C and H increase in stability with temperature while the others do not, consistent with decreasing loopgain allowing them to satisfy the thermal stability criterion that D,E,F,G have already met. 27
5.4 A reminder of the issue seen in the Aluminum that we can plausibly investigate. The early cutoff in the plot is due to a limitation of the equipment's ability to put large currents through the device. However, the large slope in the transition region was unexpected. 28
5.5 The two main models attempted, with fits given for a sample A-type detector. 29

5.6 The best fit of a line to the A type detector, which had no currently known physical motivation. 30
5.7 The 2d density plot of the best fit of a line to the A type detector. This is an important check on the validity of MCMC, as if multiple peaks had appeared more sophisticated techniques would have been necessary to accurately compare their height. 30
5.8 The histogram of MCMC point values of the best fit of a line to the A type detector. This is an important check on the validity of MCMC, which requires that parameters are roughly gaussian in likelihood distribution. 30
5.9 Fourier analysis of A-type detector for various current biases in DAC; amplitude vs. frequency. Note the "bump" of increase in frequency amplitude a bit bast 10^4. 31
5.10 Fourier analysis of F-type detector for various current biases in DAC; amplitude vs. frequency. Note the lack of a "bump" of increase in frequency amplitude a bit bast 10^4. 31
5.11 Fourier analysis of D-type detector for various current biases in DAC; amplitude vs. frequency. Note the lack of a "bump" of increase in frequency amplitude a bit bast 10^4. 32
5.12 Fitted admittance for representative type A (top) and F (bottom) bolometers. Points are measured data, one point per frequency, lines are fits to the model. Color shows the bias voltage. Data is shown down to the lowest bias voltage where the detector remained stable. . 33
5.13 Histogram of fitted γ for the A,B,E and F detectors. 34
A.1 Type A characteristic IV plot. 38
A.2 Type B characteristic IV plot. 39
A.3 Type C characteristic IV plot. 39
A.4 Type D characteristic IV plot. 39
A.5 Type E characteristic IV plot. 40
A.6 Type F characteristic IV plot. 40
A.7 Type G functional characteristic IV plot. 40
A.8 Type H functional characteristic IV plot. 41
A.9 Type A PR transition-select graph at 254mK. 41
A.10 Type B PR transition-select graph at 254mK. 42
A.11 Type C PR transition-select graph at 254mK. 42
A.12 Type D PR transition-select graph at 254mK. 43

A.13 Type E PR transition-select graph at 254mK. 43
A.14 Type F PR transition-select graph at 254mK. 44
A.15 Type G PR transition-select graph at 254mK. 44
A.16 Type H PR transition-select graph at 254mK. 45
A.17 Type A transition range graph at 254mK. 46
A.18 Type B transition range graph at 254mK. 47
A.19 Type C transition range graph at 254mK. 48
A.20 Type D transition range graph at 254mK. 49
A.21 Type E transition range graph at 254mK. 50
A.22 Type F transition range graph at 254mK. 51
A.23 Type G transition range graph at 254mK. 52
A.24 Type H transition range graph at 254mK. 53

LIST OF TABLES

Number *Page*

5.1 Detector Stats 26

Chapter 1

MOTIVATION AND INTRODUCTION

The Bock Observational Cosmology Group at Caltech is attempting to find a particular signature in the Cosmic Microwave Background (CMB): the B-Modes that are created by gravitational waves [5]. A successful detection and characterization of these B-Modes would provide an enormous amount of information about the physics of the inflationary era, the brief period in which the universe expanded superluminally [10].

However, the signal may be extremely faint, and possibly non-existent on large degree angular scales. The state of the art detector astrophysical imaging in the millimeter waves is the Transition-Edge Sensor (TES) bolometer[11] [1]. CMB measurements are currently limited by a foreground of galactic dust[16][12][4], as illustrated in Fig. 1.1 which can be subtracted by imaging at higher frequencies where the CMB is dim such as the 200-300GHz atmospheric band. The 220/270 GHz series the Bock lab has introduced to perform this imaging experienced newfound issues with thermal stability, which this thesis investigates.

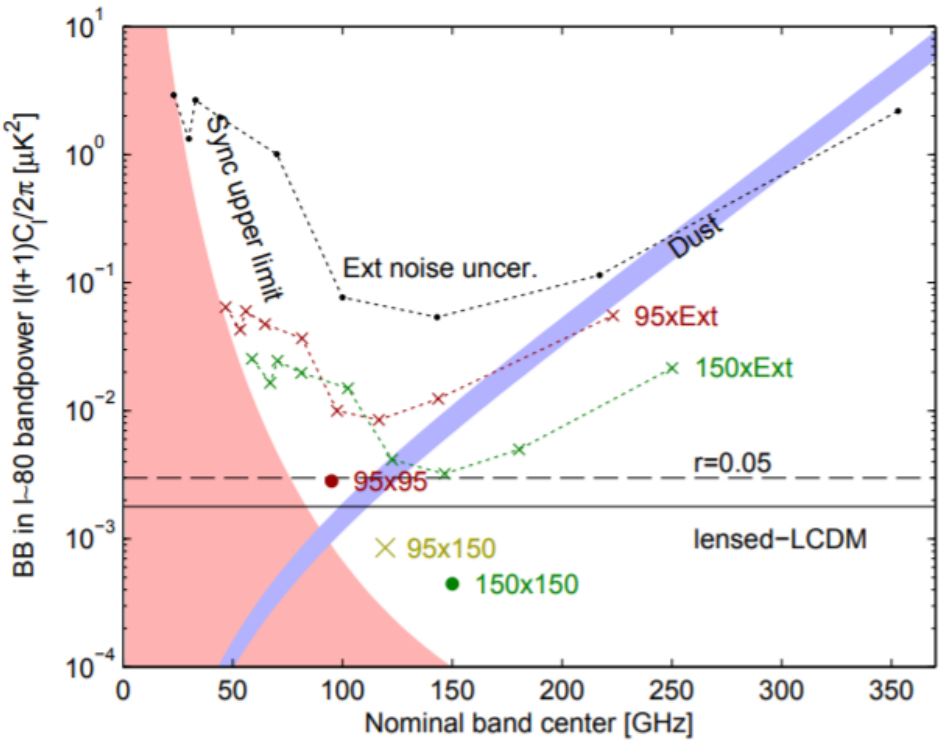

Figure 1.1: This plot of "signal strength/CMB signal strength" as a function of frequency shows the latest noise constraints on the B-mode signal, accompanied by the latest bounds on the signal's magnitude. The red patch shows allowed false-signal magnitudes of synchrotron radiation. The purple band shows allowed false-signal magnitudes from dust. The horizontal black lines are upperbounds on the B-mode signal's magnitude. Note how they have lowered enough that there is essentially no avoiding both the dust and synchrotron radiation errors, and one must be subtracted out regardless of what frequency the signal is pursued at. As the dust model is better constrained, it was chosen to use for subtraction. The 220/270 GHz range has negligible synchrotron radiation noise while still being somewhat close to the primary data taking range around 150 GHz, and thus is ideal for imaging the dust. Image Credit [4]

Chapter 2

BACKGROUND, ISSUE AND THEORY

2.1 Transition Edge Sensor Bolometers

Basic bolometers are devices that measure incident radiation (see Fig. 2.1). The radiation heats an absorber; because the material is only weakly connected to the bath (thermal reservoir), this raises the temperature of the absorber (and thus the amount of power flowing through the thermal link) until thermal equilibrium is reached with the bath. The temperature of the absorber is measured to determine how much power is being deposited on the bolometer.

A Transition Edge Sensor (TES) bolometer is a device that measures power of incident electromagnetic radiation by heating (via bias wires) a superconductor to keep it at its critical temperature (see Fig. 2.2), where it has extremely temperature-dependent electrical resistance [17]. The amount of electrical power needed to have it maximally vary in resistance is what is measured during normal operation; less power is required if the bolometer receives more optical power.

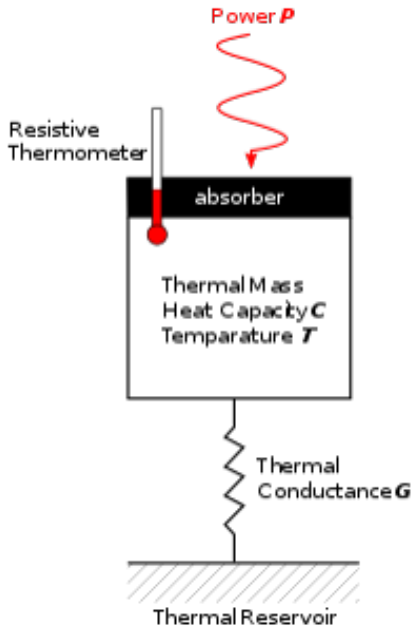

Figure 2.1: Basics of bolometers. Image credit: D.F. Santavicca, licensed under Creative Commons Attribution 3.0

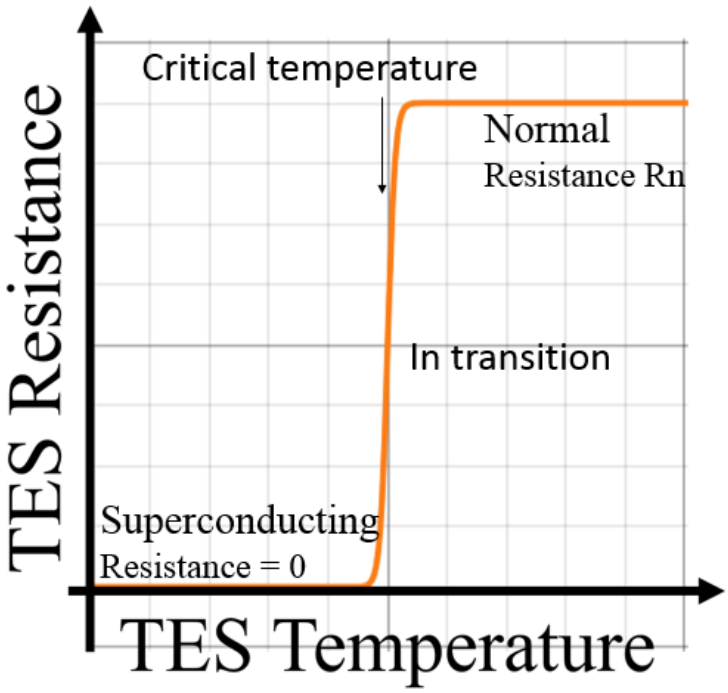

Figure 2.2: Superconductor Temperature vs. Resistance.

2.2 The IV and PR curve of the Ideal TES

We explain and derive the Ideal TES IV and PR curves, as illustrated in Fig. 2.3. Begin with the outside-transition regions.

As indicated in figure 2.2, the TES has zero resistance while superconducting. This causes all of the current to flow dissipationlessly through the superconductor (and none of it through the shunt resistor), with $I_{TES} = I_{bias}$. While our measurement system does capture this proportionality (while not clearly visible due to the differently scaled axes, the slope of the line in this region is 1), the sudden jump in current as the TES latches superconducting messes up the calibration that holds in all above-superconducting currents, causing it to be off by a constant (hence why it doesn't go through 0). This off-by-constant data (and the fact that the TES actually has 0 resistance) means this portion of the PR curve is meaningless, except to show that the transition has ended.

As indicated in figure 2.2, the TES has constant, normal resistance above a certain temperature. It thus obeys Ohm's law for the IV and PR curves in these regions.

Now, the critical transition region that is used for data taking. In the ideal TES, two circuits, thermal and electrical, combine to create negative feedback. We derive the

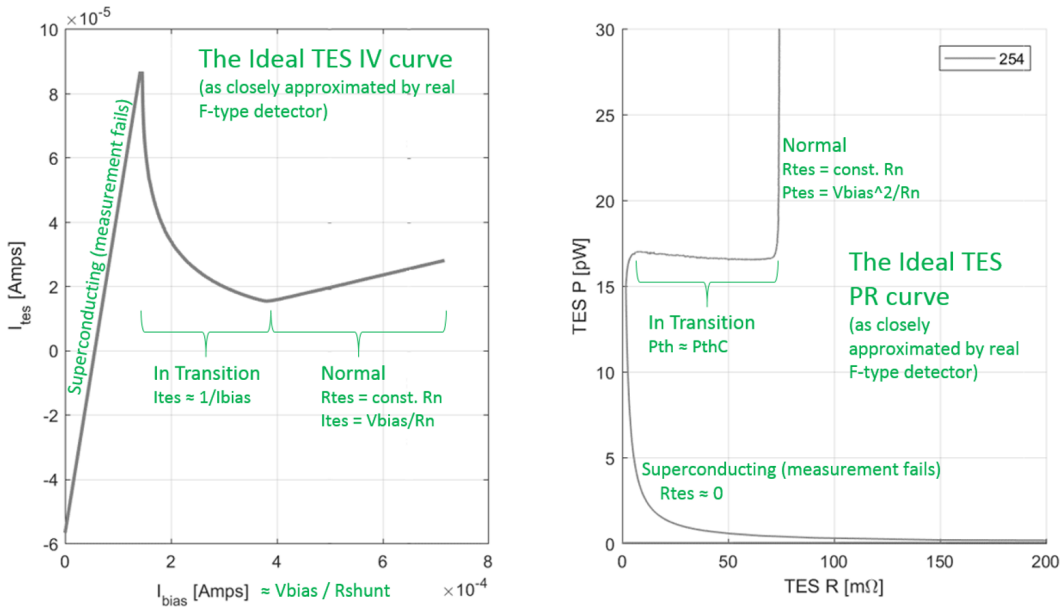

Figure 2.3: The ideal IV and PR curves, as illustrated by one of our detectors after the instability issue was fixed.

characteristic in-transition IV curve for our TES, assuming it was ideal.

Start with the thermal circuit depicted in black in Fig. 2.4. The thermal differential equation is, by the definition of heat capacity:

$$C\frac{dT_{TES}}{dt} = -P_{th} + P_{opt} + P_{el} \tag{2.1}$$

The appropriate thermal conductance equation for P_{th} is [11]:

$$P_{th} = K(T_{TES}^{n} - T_{bath}^{n}) \tag{2.2}$$

where K = $G/(nT_{TES}^{n-1})$, G = the dynamic thermal conductance = $\frac{dP_{th}}{dT_{TES}}$ and n = β + 1, β the thermal conductance exponent [15]. Our TES n is 3.5 ([1] gives β but calls it n). Importantly, $\frac{dK}{dT_{TES}}$ = 0; this can be seen by taking the derivative of Eq. 2.2. Consequently, for small signals near Tc = Titanium critical temperature, we can take the first order Taylor expansion and obtain

$$P_{th} \approx P_{thC} + G(T_{TES} - T_{bath}) \tag{2.3}$$

where P_{thC} is P_{th} when the superconductor is at its critical temperature T_C.

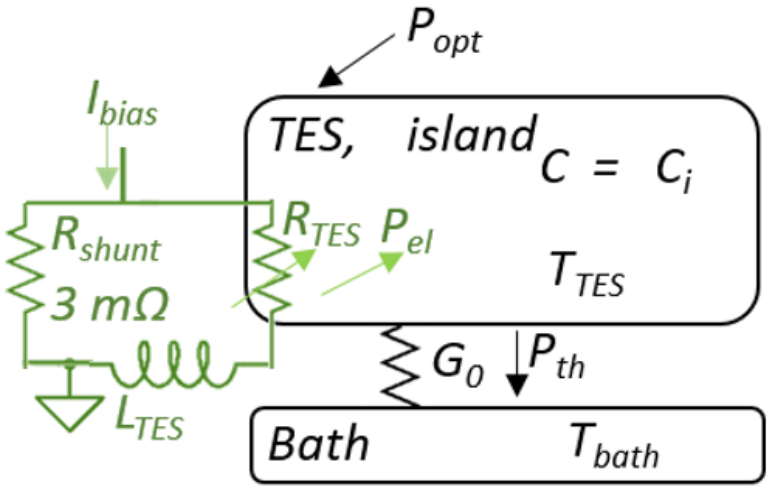

Figure 2.4: Ideal TES thermal and electrical circuit. In the ideal case, the island and the TES are much better connected than the link through the island's legs to the bath, and thus they are at the same temperature, and the island's is the only relevant heat capacity because it dwarfs the TES's.

Now consider the ideal electrical circuit, depicted in green in 2.4. For our IV curves, we run DC current, so the inductor is negligible; in the ideal case the inductor also has 0 resistance. Then V on each branch of the green electrical circuit is

$$V = I_{bias} * (\frac{1}{\frac{1}{R_{shunt}} + \frac{1}{R_{TES}}}) \tag{2.4}$$

For our detectors, $R_{TES} >> R_{shunt}$ in the transition range, so V is effectively independent of R_{TES}, and close to proportional to I_{bias}. This is the "V" in the phrase "IV curves," which looks at the current through the TES as a function of the voltage applied to it, at a given temperature. So since $P_{el} = V^2/R_{TES}$, we have that:

$$P_{el} = V^2/R_{TES} = \frac{Ib^2 R_{shunt}^2 R_{TES}}{(R_{shunt} + R_{TES})^2} \tag{2.5}$$

Eq. 2.5 captures the most critical facet of a functional TES, electrothermal feedback. As the power delivered to R_{TES} (either electrically or optically) increases, T_{TES} increases, so R_{TES} increases (as per Fig. 2.2), bringing down the power dissipated in it and returning the temperature to T_C. As the power delivered to R_{TES} (either electrically or optically) decreases, T_{TES} decreases, so R_{TES} decreases (as per Fig. 2.2), bringing down the power dissipated in it and returning the temperature to T_C (in practice, it just stays at about T_C, but more or less current runs through the TES

depending on how much power the TES is receiving from the varying optical or bias power.).

Now, since in equilibrium (and our device has time to reach equilibrium during each point in the IV curves) $P_{th} = P_{opt} + P_{el}$, and as we just explained the device stays at about T_C while in the transition region, and since our IV curves are a dark run with non optical power, and with reference to Eq. 2.3:

$$P_{thC} + G(T_{TES} - T_C) = P_{thC} = P_{opt} + P_{el} = P_{el} \tag{2.6}$$

Which we can solve to obtain

$$R_{TES}(I_{bias})@(T_{TES} = T_C) = \frac{-2P_{thC}R_{shunt} + I_{bias}^2 R_{shunt}^2 - \sqrt{-4I_{bias}^2 P_{thC} R_{shunt}^3 + I_{bias}^4 R_{shunt}^4}}{2P_{thC}} \tag{2.7}$$

Then $I_{TES} = V/R_{TES}$. I_{TES} evaluates as given at the top of Fig. 2.5.

The ideal PR curve is a flat line in the transition region, as can be seen by plugging in the appropriate values for P and R.

On-sky measurement thus compares the amount of power that must be supplied via bias to keep the TES at its critical temperature to the measured $P_{thC} = P_{Saturation}$ for the given focal plane (bath) temperature with no optical power. The less power that needs to be supplied, the more optical power the detector is recording.

Two other particularly important qualities for our TES's are α and the $\mathcal{L}$.

The resistive transition sharpness parameter α measures steepness of the transition at the critical temperature (reference Fig. 2.2):

$$\alpha = \frac{d(log(R))}{d(log(T))} \tag{2.8}$$

$\mathcal{L}$ is the DC (current) loopgain:

$$-\frac{\delta P_{el}}{\delta P_{opt}} = \mathcal{L} = \frac{\alpha P_{el}}{GT} \tag{2.9}$$

These two parameters are derived in depth in [8] and [11].

$$\text{ITESatTc}[Ibias\_,\ Rshunt\_,\ PthC\_] := \frac{2\ Ibias\ PthC\ Rshunt}{Ibias^2\ Rshunt^2 + \sqrt{Ibias^2\ Rshunt^3\ (-4\ PthC + Ibias^2\ Rshunt)}}$$

```
Plot[ITESatTc[Ib*10^-4, 3/1000, 16*^-12]*10^5, {Ib, 1, 4},
 AxesLabel→{"Ibias [A*10^-4]", "Ites [A*10^-5]"}]
```

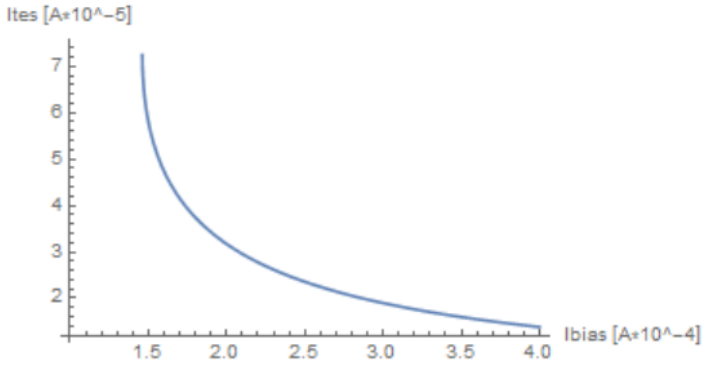

Figure 2.5: Results of derivation of Ideal TES, and also a comparison of ideal case to post-thesis modification reality. Compare to the bath temperature = 254mK run of the F type detector given in Fig. 2.7 (this specific run is reproduced here below this caption for easy comparison); this run had a $P_{thC} \approx 16$ pW which you can see from the PR curve in the right graph in this figure. $R_{shunt} \approx 3$ mΩ for our detectors. Compare this ideal PR curve to the actual PR curve for this run, the rightmost IV curve in the left graph of Fig. 2.7 (reproduced below). The general 1/x shape is correct for the in-transition region, as are the approximate magnitudes at each endpoint of the in-transition region.

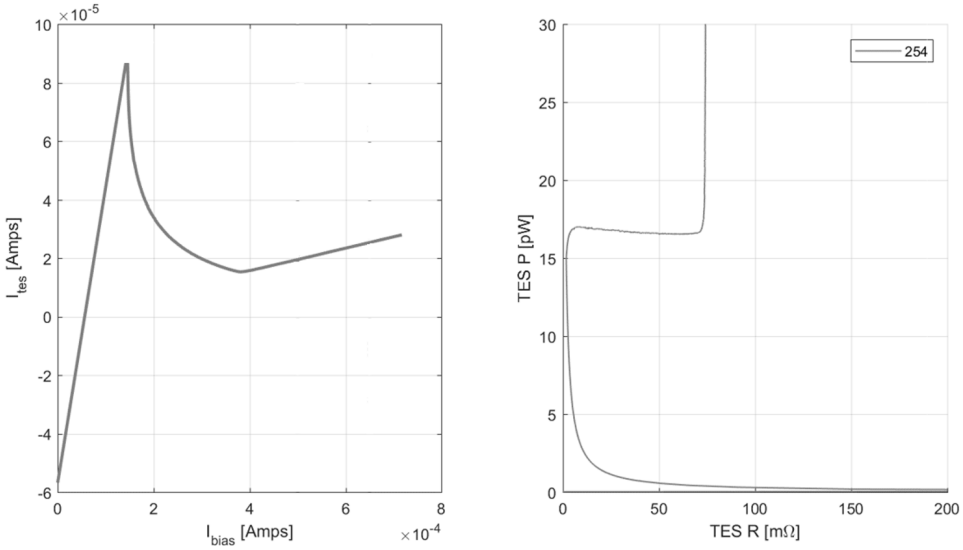

2.3 Thermal instability issue

This thesis was prompted by the fact that the original 220/270 GHz detector design did not sufficiently conform to the ideal.

The bolometer thermal conductivity G used for 270GHz imaging in a ground based experiment must be higher than that used for 95,150 or 220GHz due to the increased atmosphere temperature; more power is incident on the detectors, so more must be vented to keep them at critical temperature. In the detectors designed for the Keck experiment at 270GHz, we found that the stable operating region for these higher G detectors was limited, and the detectors would latch if operated at fractional resistances less than $\approx 50\%$ of the normal resistance, as shown in Fig. 2.6; compare Fig. 2.7.

While individually our detectors have high yield, when they are multiplexed into a large format array using a time multiplexing system (in which each detector is read out one at a time in sequence), the yield is limited by the requirement that a column of 32 detectors is DC biased with a single bias voltage. Variations in detector properties and optical loading across the focal plane cause variations in the optimal bias point for the detectors. In the lower frequency instruments, the stable regions were wide enough that the constant voltage within a column requirement did not impact yield. In contrast, the limited stability of the 270GHz detectors precluded operation of all the detectors in a column at a single bias. In the dark measurements presented here, even with no optical power variations, the simultaneously biased into transition yield was at best 67% for the baseline detector design, as shown in Fig. A.17.

In an ideal bolometer, the bolometer is connected directly to a cold bath that it

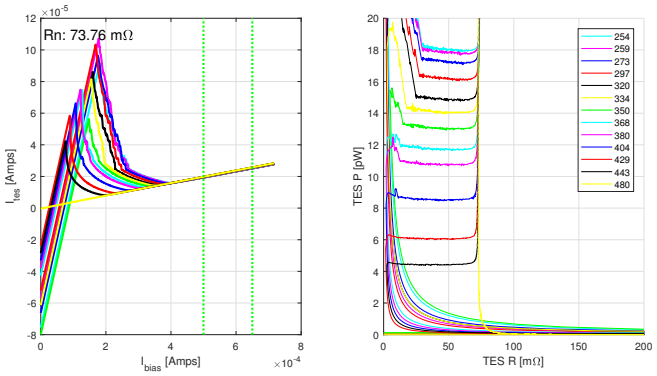

Figure 2.6: Original (type A) detector characteristic IV and PR plots.

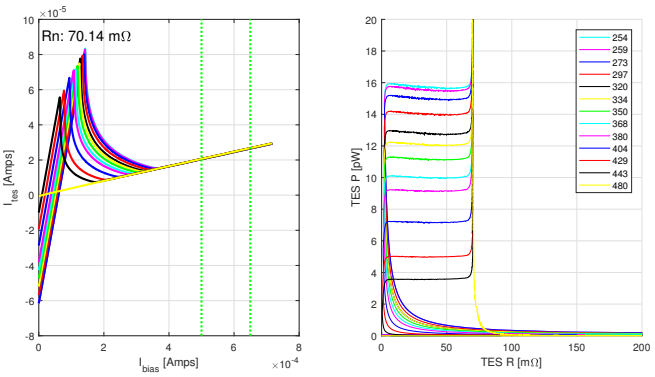

Figure 2.7: Fully functional (type F) detector IV and PR plot.

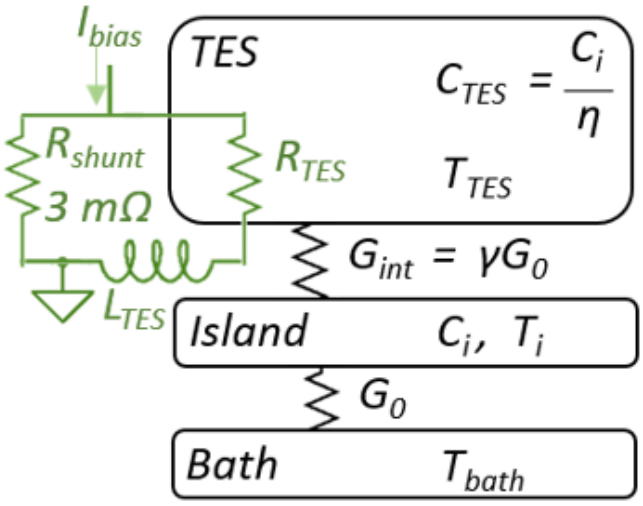

Figure 2.8: Bolometer thermal (black) and electrical (green) circuit.

vents its heat out of as per the heat equation [8]. In practice, there is more than one material the heat must flow through to reach a bath with sufficient heat capacity. This is irrelevant if these connections have sufficiently different thermal conductivities that the system is effectively modeled by only considering the lowest. However, the 220/270 GHz needed to have higher island-bath leg conductivities in order to vent the greater heat from the higher frequency light. Upon observing the instability issue, and inspired by the work of George et al [6], it was theorized this increase was enough to effectively split the bolometer thermal circuit into a two-stage system, as illustrated in Fig. 2.8; thus that the stability of the detectors was limited by the TES-heat capacity coupling, rather than limited electrical bandwidth[11].

In this model, detector stability requires that the ratio γ of thermal conductivity within the island between the titanium TES and the palladium-gold (PdAu) heat

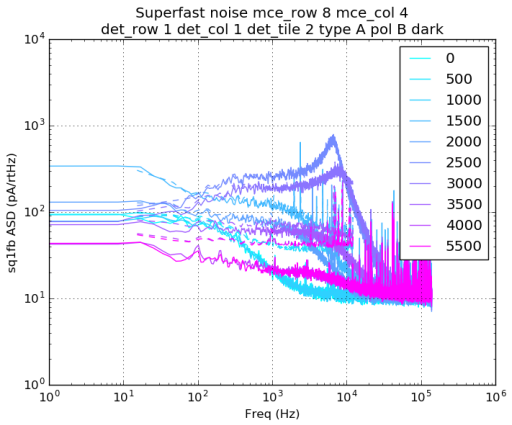

Figure 2.9: Original SF data that helped prompt this thesis.

capacity to G be greater than the electrothermal feedback loopgain. Increasing the detector G for higher frequency detectors without changing the island design decreased γ to a point where it fell below the loopgain achievable from the steepness of the superconducting transition. The thermal circuit of this model is depicted in Fig. 2.8, and leads to the following stability criterion:

$$\mathcal{L} < \gamma + 1 + \frac{C_{TES}}{G\frac{\gamma}{\gamma+1}\tau_e} \approx \gamma. \tag{2.10}$$

C_{TES} is the heat capacity of the titanium TES and τ_e is the electrical time constant of the readout circuit L/R. The term $\frac{C_{TES}}{G\frac{\gamma}{\gamma+1}\tau_e}$ is negligible because $C_{TES} << C_i$, so $\frac{C_{TES}}{G} << \frac{C_i}{G} = \tau_0 < \tau_e$, where C_i is the heat capacity of the bolometer island.

Part of what made us suspect that the two-stage system thermal instability was the cause of our odd IV curves was a superfast analysis on the original, flawed detectors, that revealed a surprising upwards peak at a bit past the R_{shunt}/L value (L for us is 1.35 μH), as depicted in Fig. 2.9. This seemed to indicate the circuit losing electrothermal feedback and oscillating unstably.

2.4 Bolometer decoupling model

We considered two possible mechanisms for the internal thermal resistance of the island: Thermal resistance due to the small cross sectional area of the island the TES and PdAu are mounted on (see Fig. 2.10), and a thermal resistance between the quasiparticles in the superconductor and the phonons.

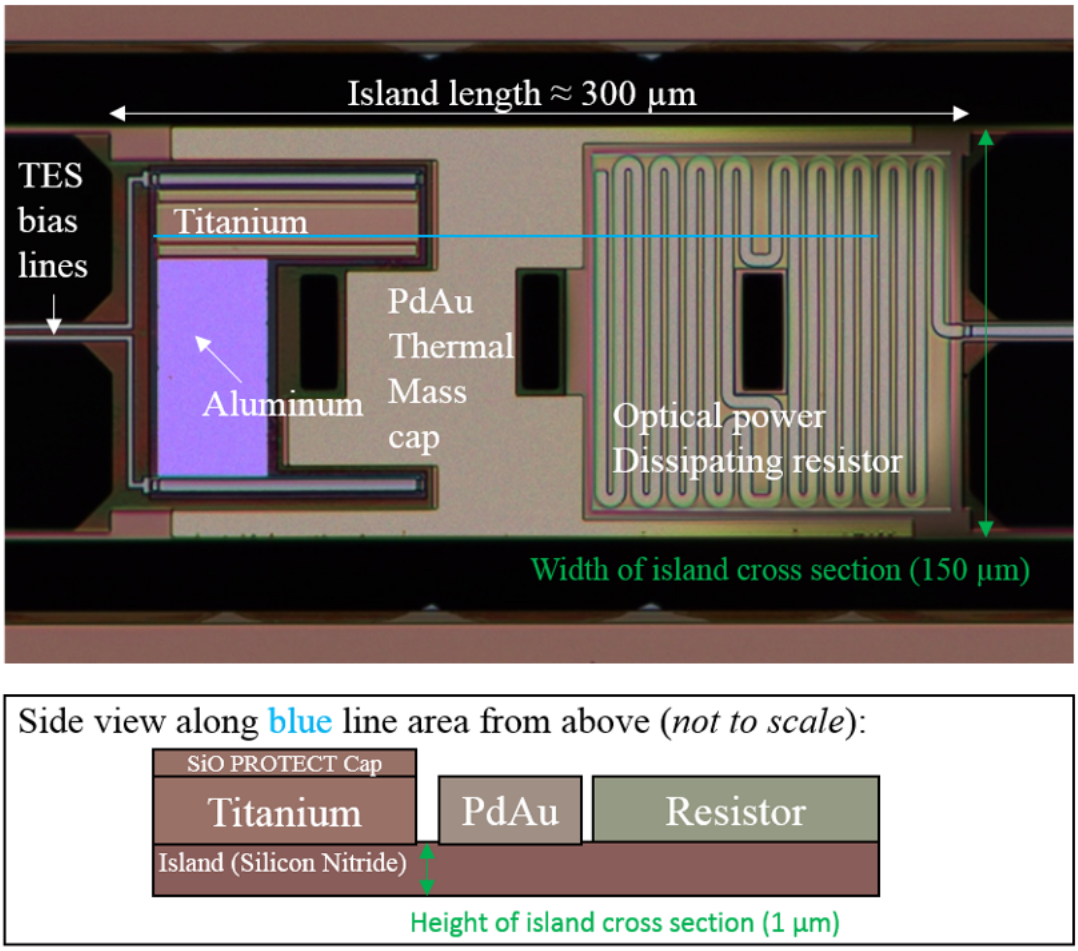

Figure 2.10: Above: Annotated photograph under microscope of a control group (A-type) detector. Below: Diagram of side view along blue line on the photograph, not to scale. In green: location of the relevant 150 μm^2 island cross section. Note the green dimensions line on the photograph had to be moved to the side; the side view green dimension line shows the relevant location along the island's length.

The thermal conductance of a rectangular aperture of an insulator reaches a limiting value as the insulator gets thinner, determined by the Stefan-Boltzmann law for radiation. The limiting value in silicon nitride has been shown to be consistent with this model[9][20]:

$$G = 4\Sigma AT^3 \tag{2.11}$$

Where G is the thermal conductance dP/dT, Σ is the Stefan-Boltzmann constant for phonons in silicon nitride of $15.7 mW/cm^2K^4$, and A is the cross sectional area. The cross sectional area of our island is $\approx$150 μm^2, and all the heat between the TES

and the PdAu heat capacity must pass through this small aperture for the baseline A type detector (see green text in Fig. 2.10 for relevant cross section location.). For the titanium transition critical temperature $T_c = 0.5K$, this is a decoupling thermal conductance of $G_{int} = 12nW/K$. For a typical leg thermal conductivity $G \approx 150pW/K$, $\gamma \approx 80$, and stable detector operation will be limited to loop gain $\mathcal{L} < 80$.

The heat capacity of the titanium TES we estimate at $C_{TES} = 0.016pJ/K$ from its volume, $100\mu m^3$, the critical temperature of our titanium films $T_c = 0.50K$, and the bulk electronic heat capacity of titanium, 310 $Jm^{-3}K^{-2}$. The island heat capacity we estimate $C_i = 4.8pJ/K$, from the measured bolometer τ_0 and G. Because C_{TES} is so small compared to the C_i, we neglect including it in the model for the bolometer impedance.

A second possibility for the thermal resistance is the electron-phonon coupling, i.e. hot electron effects. Measurements of the electron phonon relaxation time in titanium films[7][19] give 1-3 microseconds at 0.5K, though in films with $T_c < 0.5K$. Given a TES volume of $\approx 100\mu m^3$, $G_{e-ph} = 6 - 17nW/K$, or $\gamma = 40 - 110$. G_{e-ph} and G_{int} are quite similar but we can distinguish between them by modifying the bolometer to bring the palladium-gold closer to the TES with or with out direct electrical contact.

2.5 Modification Logic and Designs

As per Eq. 2.10, in order to stabilize, we must either increase γ (decrease the internal thermal resistance of the island) or decrease the loopgain $\mathcal{L}$. We prefer the former, as high loopgain enables faster measurements, but will also investigate the latter.

If G_{int} is the main bottleneck, we can increase γ by layering PdAu over either the Titanium or the Aluminum, or both. This adds surface area such that heat can dissipate through the oxide coatings on the two metals straight into the PdAu heat capacity, without having to go through the island cross section.

We can also make direct electrical contact between the PdAu and the TES (by cutting away the oxide cap). This removes an insulating layer and allows electrons to directly interact with the gold, which would solve the thermal instability issue if G_{e-ph} is the main bottleneck. Note multiple cuts cannot be connected by PdAu, as that would short the TES.

This direct electrical contact would also “poison” the superconductivity of parts of the circuit, as proximity effects would weaken the superconductivity and thus the

loop gain. We can fill several cuts with PdAu if we don't connect them to the main PdAu deposit or each other. We thought we couldn't (cost-effectively) cut through the oxide over the Titanium without also cutting up the Titanium, but two designs (E and G) with this cut were attempted anyway.

To test if internal thermal conductivity was responsible for limiting our detector stability, we manufactured a wafer of detectors with eight modifications to the layout of the TES and heat capacity, based on the above logic. Fig. 2.11 shows the eight different styles we tested. They explore different connections to the aluminum TES and titanium TES.

- A - The original detector design, described in Fig. 2.10. The control group.
- B - A finger of palladium-gold is extended over the aluminum TES (T_c = $1.5K$), but not the titanium TES, separated by oxide. Checks whether heat is flowing through the superconducting Al (normally, it shouldn't, so we expect these to be identical to the control group for Ti testing). If the Aluminum TES curves also display the control group thermal instability problem (less likely due to the higher Aluminum critical temperature decreasing loopgain, making it easier to satisfy the stability condition from Eq. 2.10), it checks whether additional non-electrical-contact surface area will solve the issue in the Aluminum (and thus if the island cross section is the bottleneck).
- C - Like B, but with a via through the oxide to allow direct electrical contact between palladium-gold and aluminum. If the Aluminum TES curves also display the control group thermal instability problem, it checks whether additional electrical contact can solve the problem (indicating by comparison to type C, and to bias impedance loopgain measurements, if electron-phonon conversion is the main bottleneck).
- D - A finger of palladium gold is extended over the titanium TES, separated by oxide. Checks whether additional non-electrical-contact surface area will solve the issue in the Titanium (indicating that the island cross section is the main bottleneck).
- E - Like D, but with a via through the oxide down to the titanium. Checks whether additional electrical contact can solve the problem (indicating by comparison to type D, and to bias impedance loopgain measurements, if electron-phonon conversion is the main bottleneck in the Titanium.).

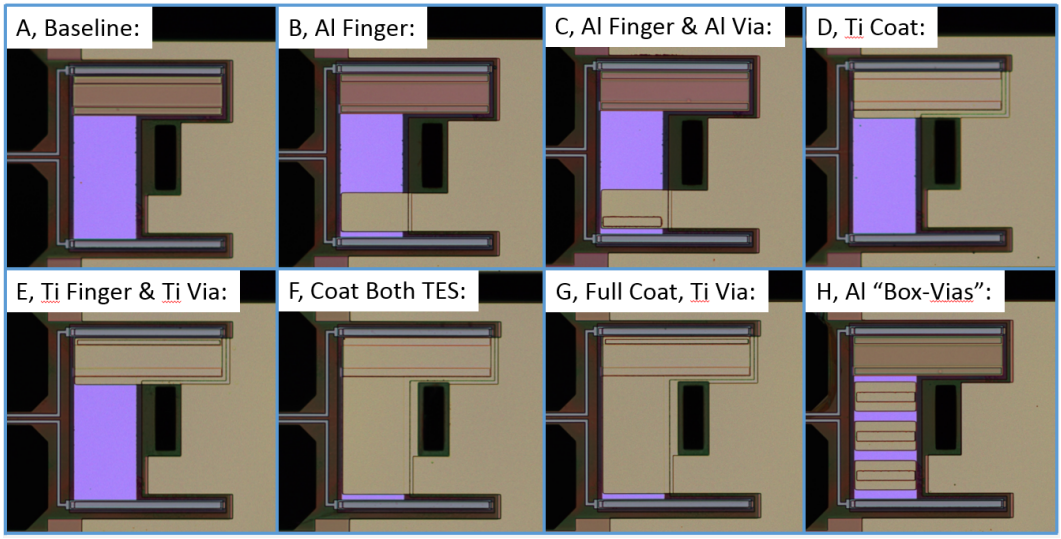

Figure 2.11: Photographs of the 8 bolometer designs.

- F - Palladium-gold covers both aluminum and titanium TES, separated by oxide. Checks whether additional heat capacity makes any difference. Provides additional width in the cross section for heat flowing out of one metal to reach the main PdAu cap, but could in theory allow easier thermal transfer between the two TES's.

- G - Like F, with a via through the oxide down to the titanium. The combination of large width-cross section thermal coating, plenty of heat capacity, and electrical contact to the Ti should produce the greatest increase in G_{int}. If this design did not get rid of the thermal instability in the titanium (though possibly harming the superconductivity), the entire approach was somehow fundamentally flawed.

- H - Short sections of palladium-gold with vias down to the aluminum, unconnected to the main heat cap. Checking if vias alone (unconnected to the thermal circuit) caused any problems.

One wafer of 128 detectors was fabricated with sixteen bolometers of each of these types.

2.6 The Aluminum PR curve investigation

When the IV and PR curves were calculated for the Aluminum regime ($T_C \approx 1.2$ K), two unexpected features emerged.

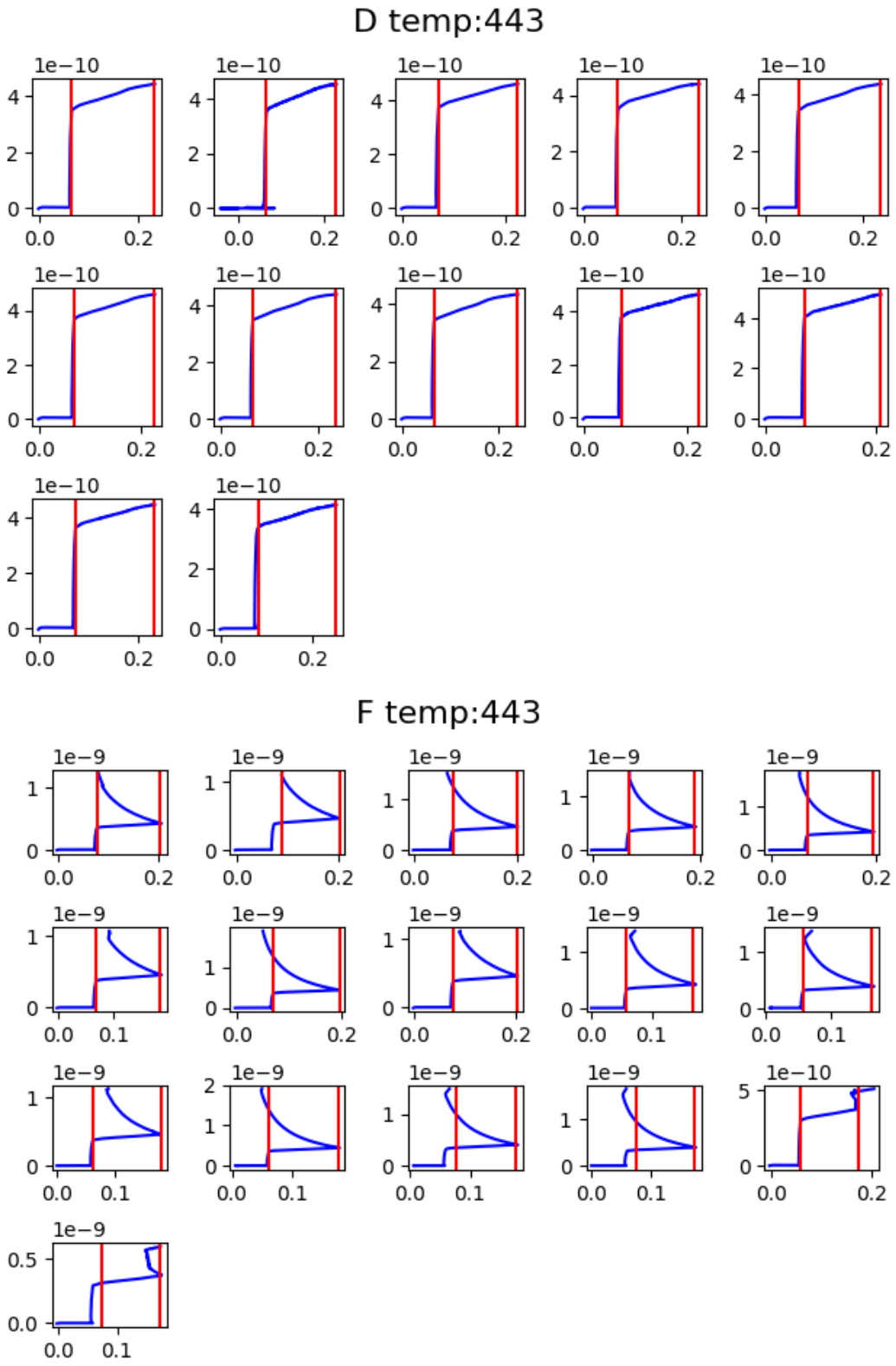

Figure 2.12: The cuts of the aluminum transitions for the type D (above) and type F (below) detectors. Red lines mark the start and ends of the selected transition region from the data (blue). Note the differences in how the transitions end.

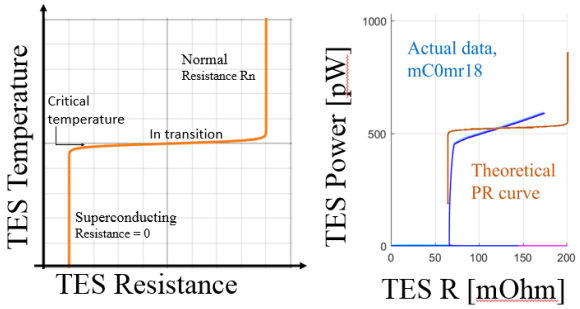

Figure 2.13: The early cutoff in the plot is due to a limitation of the equipment's ability to put large currents through the device. However, the large slope in the transition region was unexpected.

First, there was noticeable variation in the transition ending of the detectors between types. For example, Fig. 2.12 are the transition cuts of the functioning D-type and F-type detectors (the two leading contenders for the lab's choice of future design, with F previously favored before this analysis due to its higher yield). The exact patterns displayed in these end steps are likely artifacts of the SQUID (Superconducting Quantum Interference Device) losing its tracking and calibration due to some unexpected behavior of the Al TES. Unfortunately, that means there is not much merit to attempting to analyze them directly in this analysis.

Second, every functional Aluminum detector had a nontrivial slope in the theoretically flat PR transition, as illustrated in Fig. 2.13. Note that the equipment we had available was primarily designed to look at the Titanium and it was expected that it would not get all the way into the Al transition, hence the failure to reach the R-normal upturn. Nonetheless, an excessive slope is problematic as the device's sensitivity depends on the sharpness of the slope (In particular, this corresponds to a low α). Thus we investigated some possible explanations for this slope.

Some relatively plausible models considered for the Aluminum:

- Phase separation is occurring in the TES due to our Aluminum TES's relatively long length [2]. Then instead of a TES in transition (see Fig. 2.13), we have part of a TES superconducting and the other part normal. Heat is not dissipated in the superconducting region due to its 0 electrical resistance. Thus, the longer the normal region, the more area for thermal contact between it and the island, and the total thermal resistance from the TES to the island should be inversely proportional to the resistance for the TES in the apparent

"transition" region. This could also help explain the SQUID's abrupt failing to track the devices as a sudden phase transition.

- The two-stage temperature system previously considered for the Titanium TES, which was not expected to be relevant for the Aluminum TES due to the higher critical temperature and lack of empirical observation of its effects [6].
- The potential variance of the electron-phonon resistance and TES phonon-island phonon contact resistances [18]).
- The TES having a current-dependent critical temperature [3].

Chapter 3

METHODS: DATA ACQUISITION

3.1 IV curves data acquisition

The Focal Plane Unit # 1 [FPU # 1], which the detectors rest on, was cooled overnight to its lowest value of approximately 250mK. The measurement system was calibrated, and if the readout component (the SQUID attached to a given detector failed, this was noted (no data was taken for these detectors). Then, for each temperature of interest, the detectors were briefly heated to "unlatch" them before data was taken.

Exterior heating was necessary because when the TES goes far enough below its critical temperature and becomes superconducting (as it is at 250mK), its resistance becomes extremely low, and so Joule dissipation has little effect on the temperature. Thus, simply increasing the current through the device has little effect on the resistance of the TES up to a certain critical current that heats it enough to bring it from its low temperature into the transition region, and the critical current needed for detectors at 250mK is too high to practically run through the detectors. So the entire FPU # 1 was heated until the detectors were hot enough for it to be practical to apply the critical current ("zap" the detector) to pull them out of their "latched superconducting" state, past the superconducting transition region and into being simply normal resistors. Then a smaller constant bias was applied to keep them above the transition as the FPU # 1 was allowed to cool.

Once the FPU # 1 reached the desired temperature, all the detectors had the bias simultaneously and steadily decreased from 0.7 milliAmps to nothing, and the detector response was recorded. Note that in these "dark" runs the feedback equipment for keeping the detectors at their critical point was not run, in order to examine their full transition curve. Then the entire process was repeated for the next temperature of interest, as illustrated in Fig. 3.1.

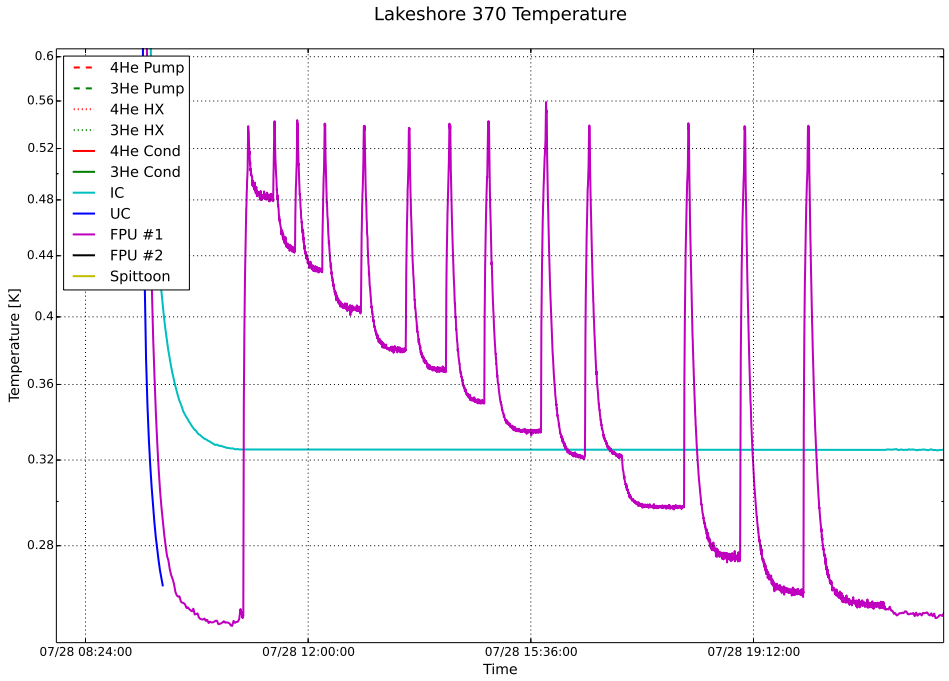

Figure 3.1: FPU # 1 temperature during the successful data-taking run is in pink. Note that the temperature of the detectors exceeds the FPU # 1 plane during the application of the critical current ("zapping") that occurred at the top of each peak, and for some time thereafter as data was taken.

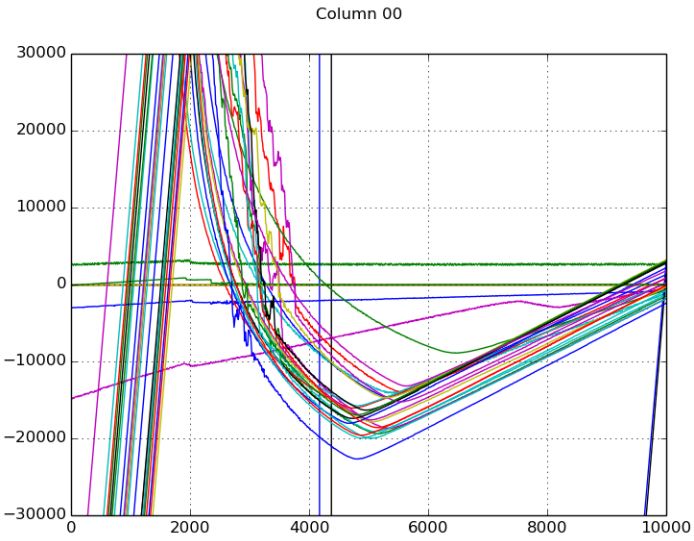

Figure 3.2: An example of raw data for some of the IV curves at 254mK. Displays I-TES vs. I-bias, each in DAC [Data Acquisition and Control units].

Calibration

The readout circuit for I_{TES} on each detector is only correct up to an offset. The actual magnitude of the currents is relevant for power versus resistance calculations, so the data is calibrated using the fact that the TES becomes a normal resistor at sufficiently high temperatures. At such temperatures, as are apparent in Fig. 3.2 from at least higher than 8000 DAC, the detector has a constant resistance value.

Referring to the circuit as documented in Fig. 3.3, each branch must have voltage $R_{shunt} * (I_{bias} - I_{TES})$. Thus by Ohm's law $R_{TES} = R_{shunt} * (I_{bias} - I_{TES})/I_{TES} = R_{shunt} * (I_{bias}/I_{TES} - 1)$.

The value of I_{bias}/I_{TES} was read by fitting a line to a region where the detector was a normal resistor, as enclosed by the dashed green lines displayed on the calibrated IV curves such as Fig. 3.4. This line's offset (the value displayed next to 'Off' at the bottom of the IV curves) was subtracted from the raw data to calibrate the offset, as per Ohm's law; this calibrated data is displayed in the IV plots shown henceforth. The I_{bias}/I_{TES} was used to calculate the normal resistance (Rn value) of the detector as described above. The average Rn over the different temperatures is displayed at the top left of the IV curves. If this average Rn was outside the range of 30-150 milliOhms, the plot was said to have "Failed the Rn cuts", because such slopes are highly unlikely to have come from functional detectors. In this data set, all such failures were unmistakably not following the typical TES IV curve. For example, many E and G types failed in the same manner as illustrated in Fig. 3.4.

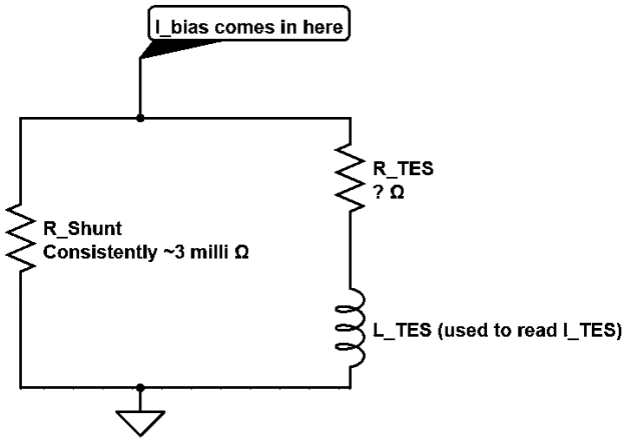

Figure 3.3: Simplified version of the TES circuit. The inductor is used to read out the circuit by projecting a magnetic field; ideally, there is only a negligible voltage drop across it when data is being read.

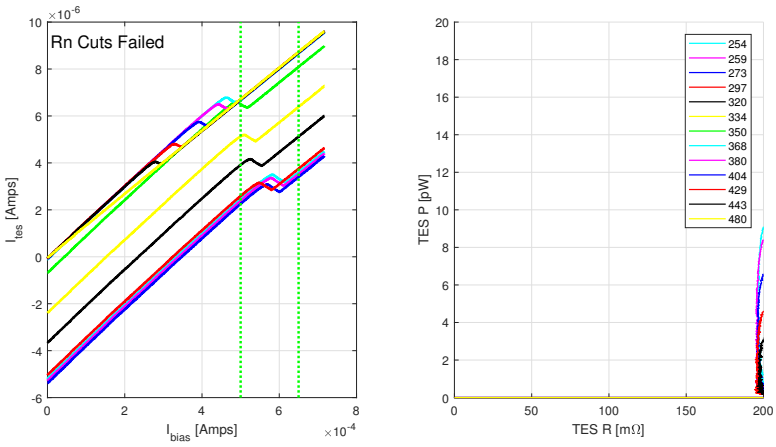

Figure 3.4: Type G "double transition" Rn failure IV plot.

Differences in Aluminum IV curve data acquisition

There was one important limitation on the Al IV curves: the bias needed reach the Aluminum normal region was beyond the equipment's capacity (though it could get high into the transition).

3.2 Superfast data acquisition

Superfast refers to taking data faster than normal (200 kHz as opposed to the 1 kHz science data taking rate). This is made possible by only taking data for one row of detectors at a time, enabling the machinery to more quickly cycle through all of its target detectors. The point is to map the detector response in the frequency domain, which is important for analyzing noise and detecting any issues with aliasing. In superfast data acquisition, the detectors were unlatched as with the IV curves, and then fed a steady DC bias current.

3.3 Bolometer impedance acquisition

To explore the mechanism of instability seen in the IV curves, we measured the electrical impedance of the bolometers.

Like Lindeman et al[14], we add a known perturbation to the TES bias voltage, and measure the response current, though we use a small amplitude square wave modulation rather than white noise. The frequency of the modulation was swept from 2.6Hz to 1.6kHz for several bias voltages over the same range used for the IV curves. Assuming linearity, the amplitude and phase of the bolometer current in the first harmonic provides a measurement of the complex impedance of the bolometer at the input square wave frequency.

Chapter 4

METHODS: ANALYSIS

4.1 Titanium TES

The Titanium TES is the main science detector, used for making measurements. After the IV curves were taken and the data was calibrated, the current data was used to construct Power-Resistance plots, as seen in the right side of several previous figures (e.g. Fig. 2.6, 2.7). This was done to find the in-transition region more easily and in accordance with the theory on superconductor transition curves (reminder in Fig. 4.1). In practice the measuring equipment is prone to difficulties and erratic behavior once the TES is too far into the superconducting zone (acceptable because while measuring science data it should not enter it), hence why the superconducting sections of our PR plots differ from theory.

Selecting the in-transition region from the PR plots was nontrivial. Picking the transition by hand was not feasible for the 1664 different detector-temperature combinations. The initial algorithm relied on a hardcoded difference in standard deviation between the next and previous 10 points. As illustrated in Fig. 4.2, this algorithm

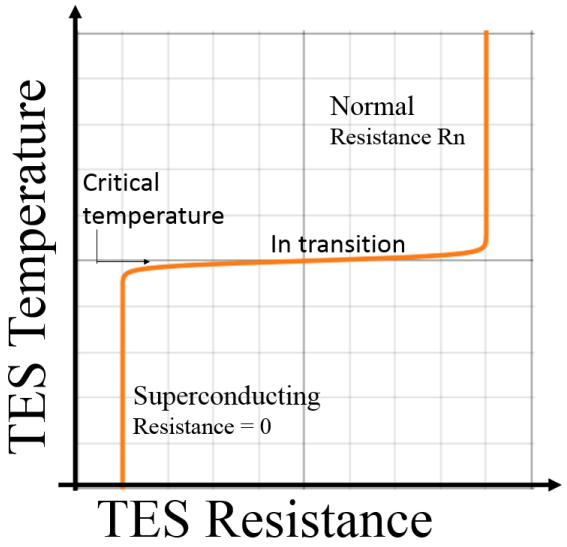

Figure 4.1: Ideal superconductor resistance curve. Note that as per the heat equation, the power dissipated in the detectors is related to the temperature of the detectors; the more power dissipated, the higher a temperature difference will be established between the detectors and bath.

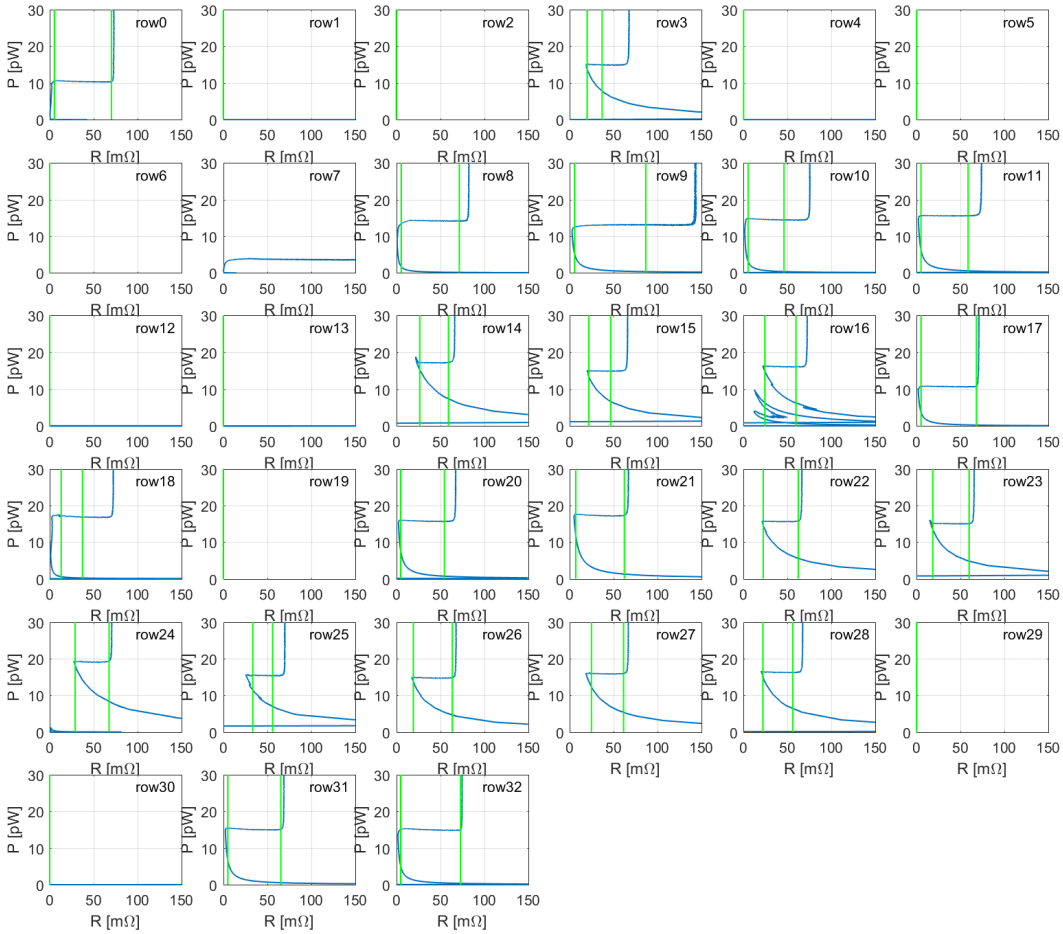

Figure 4.2: A particularly bad column (mce column 3) of Algorithm 1 (local standard deviation change) PR plot results for the 254 mK run. Consider, for example, the row 9 detector. Blank plots has failed or absent detectors, or failed SQUIDS.

was insufficiently accurate due to large differences in noise levels between detectors.

Several iterations occurred between the first and the final, successful algorithm for cutting the titanium transitions (it was successful on all but 4 detectors, which were then set by hand inspection). For comparison the final algorithm produced the cuts in Fig. 4.3

For Titanium PR transition cutting algorithm code please contact the author.

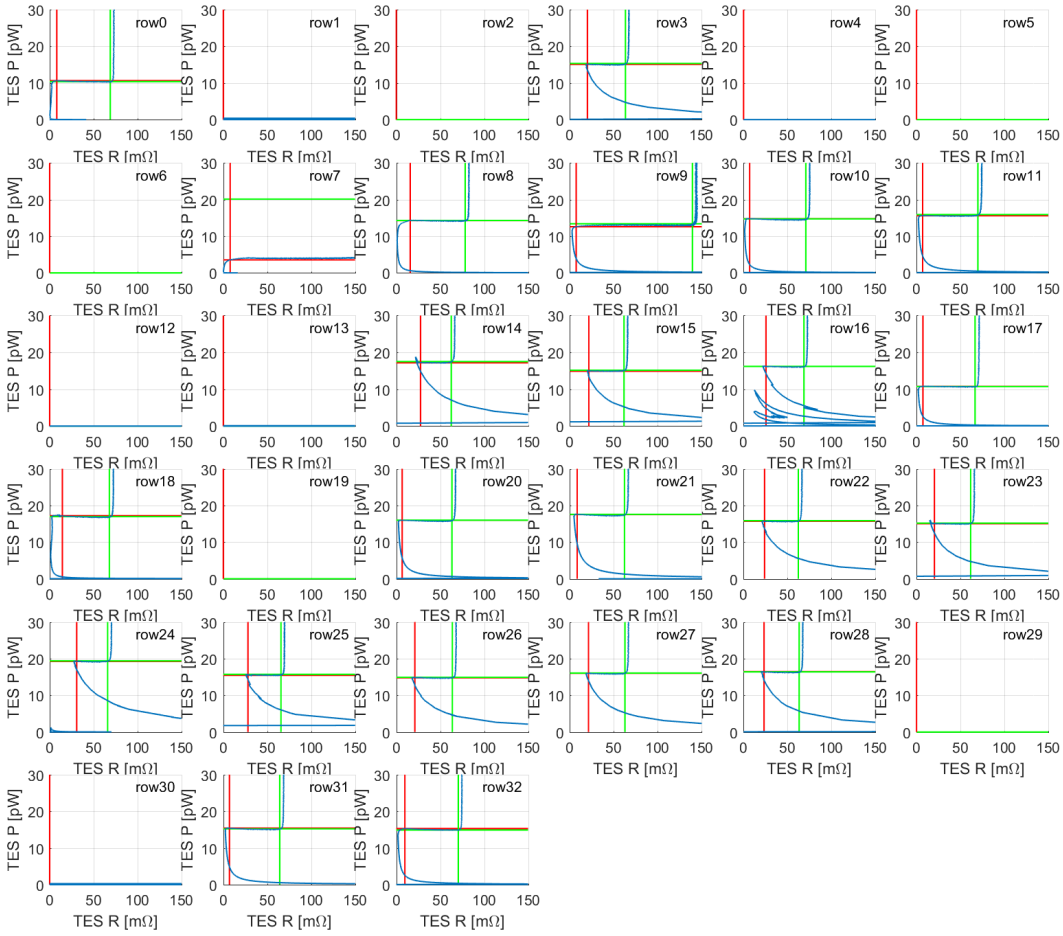

Figure 4.3: The same column algorithm 1 failed on, much improved in the final algorithm.

4.2 Aluminum TES

The aluminum TES is primarily used for calibration and testing under a 300 K background due to its higher saturation power [1].

The Aluminum also had some issues with plotting PR cuts that were eventually resolved. For Aluminum PR transition cutting algorithm code please contact the author.

Basic Statistical Methods for modeling

The bias-step response test was performed at 3 different bath temperatures, 443 mK, 475 mK, and 493 mK. These three runs were effectively offset from each other in power; thus, they were used to estimate error in the measurements by interpolating to have matching resistance points, and subtracting the average difference from one set, and then taking the standard deviation of the resulting equalized points, which

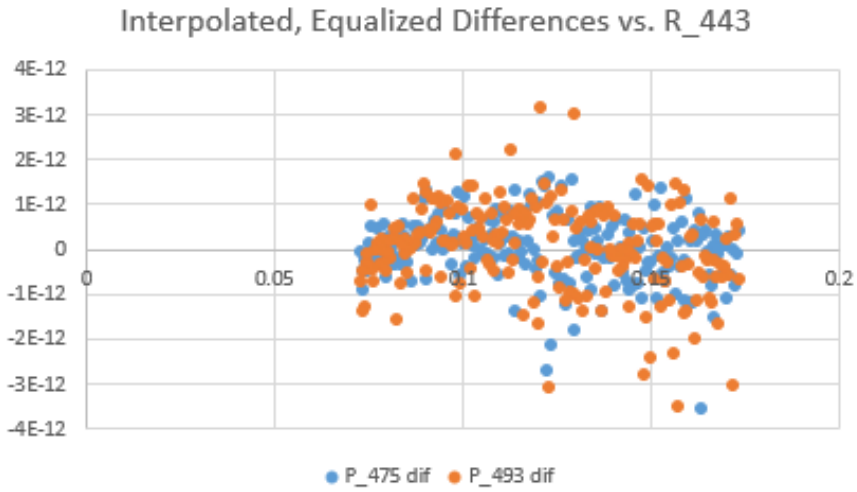

Figure 4.4: These residuals are small compared to the actual values.

are plotted below for the model detector in Fig. 4.4. The errors are two to three orders of magnitude less than the values of the points they bound. Running the fits with an additional sigma parameter did not significantly affect the shape of the best fit.

These errors were then used to find an initial starting estimate for various model parameters, which were then run through a 1 million point Markov Chain Monte Carlo to estimate a best fit and uncertainties. The resultant best fit was then taken as the new starting guess for another derivative-seeking optimal estimation in order to get the final best fit parameters. The percent of best fit parameters that were selected this way to lie within the error bounds determined by the MCMC is referred to as the optimal capture; optical capture < 100% was taken as a sign that convergence had not occurred and more steps were necessary (in all cases, enough steps did guarantee 100% optimal capture).

4.3 Superfast

The basic analytical approach is to perform a Fourier transform to see the noise at different frequencies. Detailed analysis of the superfast data beyond this has not yet been prioritized.

4.4 Impedance

We fit the complex impedance data to a model for the admittance Y that includes all three mechanisms for instability - ratio of the TES resistance to the shunt resistor,

electrical bandwidth of the readout, and thermal decoupling.

```
R = TES resistance
Lnyq = 0.7e-6 H
Rsh = 0.003 Ohm
b = L0/gamma
eps = Rsh / R
taue = Lnyq / R
t0 = -1j*(-1 + b + L0) + (-1 + b)*w*tau0
t1 = 1j*(1 + b + L0 + eps - (b+L0)*eps)
t2 = (-1 + b*(-1+eps)-eps)*tau0*w
t3 = taue*w*(-1+b+L0+1j*(-1+b)*tau0*w)
Y = (1.0/R) * t0 / (t1 + t2 + t3)

Fit parameters:

gamma: Ratio of internal thermal conductivity to leg thermal conductivity. Highe
loopgain L0: Ratio of electrothermal feedback to leg thermal conductivity. Zero
R/Rn: Fraction of normal resistance. Measure of depth in transition.
tau0 or f3db0: Ratio of island heat capacity to leg thermal conductivity. Speed
```

Like the standard model for the ideal TES, this has two time dependent degrees of freedom, the current in the TES and the temperature of the island.

The difference is that the TES temperature (T_{TES}) can heat above the temperature of the island (T_{island}) through electrical power dissipated in the TES (P_e) flowing through the decoupling link (γG):

$$T_{TES} = T_{island} + \frac{P_e}{\gamma G} \tag{4.1}$$

All the bias points for one bolometer are fit simultaneously, with a single value for τ_0 and γ, and a value per bias voltage for $\mathcal{L}$ and R.

Chapter 5

RESULTS

5.1 Titanium IV curves

An ideal detector has three regions in its IV and PR curves, corresponding to normal at high bias, in transition at intermediate bias, and superconducting at low bias. Detector instability appears as an additional region between in transition and superconducting, where the readout system fails to track the detector current. We estimate the range over which the detector is in transition by placing a criterion on the flatness of the PR curve, and looking at the difference between the normal resistance and the highest resistance where the detector is unstable.

Transition range graphs

Table 5.1 displays the critical metrics for simultaneous operation of columns of detectors derived from the data for all detector types. Figures 5.1 and 5.2 plot the transition ranges of detector types A and F and illustrate the derivation of the critical metrics. The voltage bias in the table has units of microamps of current applied to the $3m\Omega$ shunt resistor.

While the few E and G types that passed the normal resistance cuts had long mean lengths, their yields were very low, and most of their failures displayed an IV pattern unique to these types. These are the types that had vias down to the titanium to make direct electrical contact. The D and F types on the other hand had high yield,

Table 5.1: Detector Stats

Det. type	Det. yield[1]	Max Det. Simultaneously Biased[2]	Best Bias $[\mu A]$	Best Bias Region Length $[\mu A]$	Mean Length $[\mu A]$
A	83	67	317	14	105
B	88	69	280	4	100
C	92	83	280	29	120
D	93	93	247	93	170
E	46	46	246	128	190
F	100	100	225	100	169
G	31	31	272	166	178
H	100	100	313	25	126

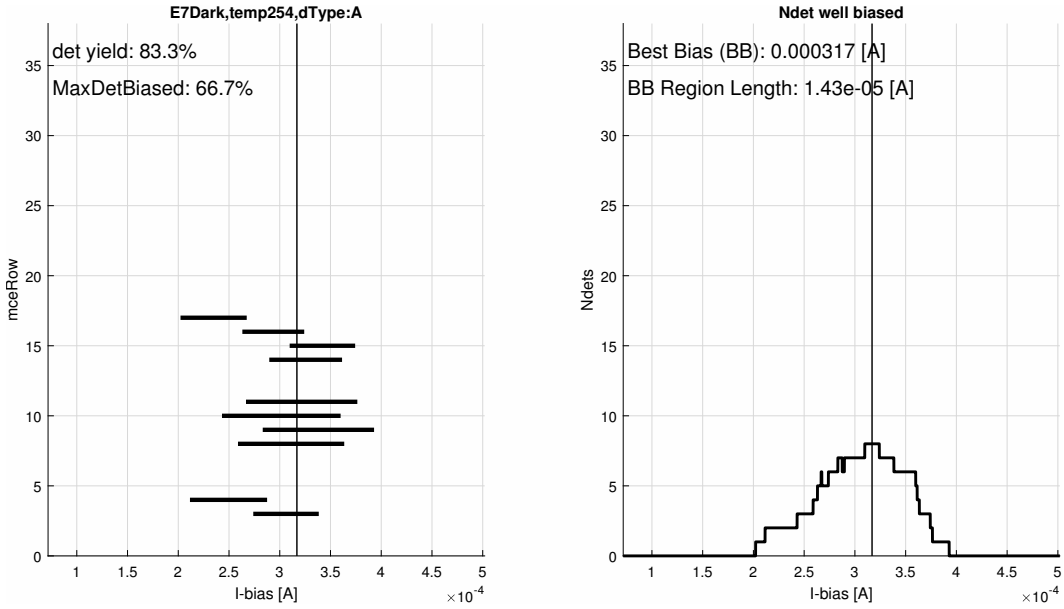

Figure 5.1: Type A transition range graph at a bath temperature of 254mK. The x axes are the current applied to the TES shunt resistors. The vertical line shows the optimal current where the largest number of detectors are operating simultaneously. In the left plot, horizontal bars show the limits of the in transition for each detector of type A. The right plot shows the count of in transition detectors for each bias current.

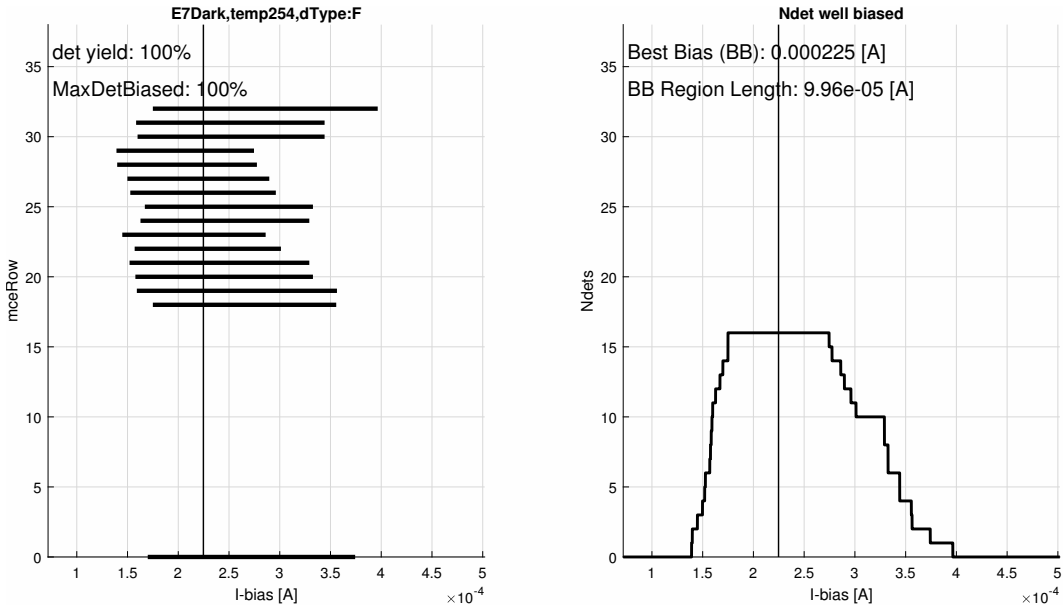

Figure 5.2: Type F transition range graph at a bath temperature of 254mK. Compared to Fig. A.17, the stable bias regions are much wider for each detector.

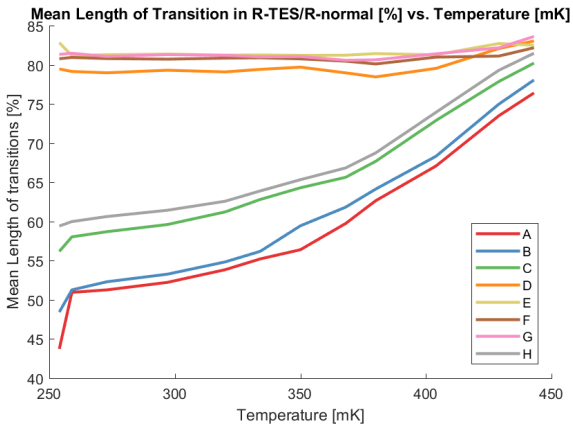

Figure 5.3: Mean length in which a detector was usable (in R_{TES}/R_n %) vs. Temperature (in mK). Higher is better. Types A, B, C and H increase in stability with temperature while the others do not, consistent with decreasing loopgain allowing them to satisfy the thermal stability criterion that D,E,F,G have already met.

and very wide biasable regions, without the characteristic instability of the baseline A-type detectors. The D and F types have no direct electrical contact between palladium-gold and titanium, indicating that the limiting thermal resistance in the A-type is the silicon nitride island thickness, and the electron-phonon relaxation time in our titanium may be shorter than 1-3 microseconds.

5.2 Aluminum PR Slope Models and Fit Results

One plausible explanation for the slope is that, instead of a normal transition curve, phase separation is occurring in the TES due to our Aluminum TES's relatively long length; Anderson et al. suggests that this effect would occur to some extent in our

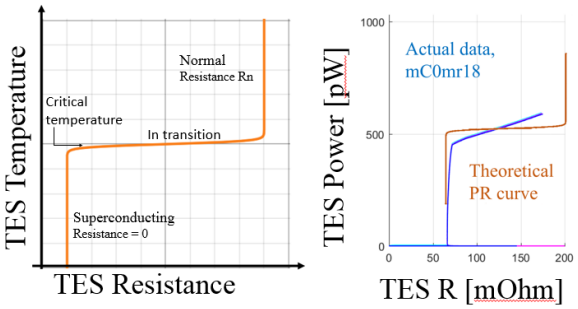

Figure 5.4: A reminder of the issue seen in the Aluminum that we can plausibly investigate. The early cutoff in the plot is due to a limitation of the equipment's ability to put large currents through the device. However, the large slope in the transition region was unexpected.

detectors [2]. Then instead of a TES in transition (see Fig. **??**), we have part of a TES superconducting (electrical resistance 0) and the other part normal (electrical resistance Rn). Thus, the total thermal resistance from the TES to the island should be inversely proportional to the resistance for the TES in the apparent "transition" region: as the normal, electrically resistive, heat-conducting region expands, the surface area of it increases and thus the total thermal conductance increases.

Fourier's law gives that $P_{thermal} = P_{th} = (T_{TES} \check{} T_{bath})/R_{thermal} = P_{electrical} = P_{el}$ in electrothermal equilibrium. The thermal resistance comes from two thermal resistances in series: the thermal resistance of the TES to the island it rests on, and the thermal resistance of the island's legs that connect to the bath. The temperature of the bath was constant; we model the temperature of the TES as constant at the Aluminum critical temperature (1.5 K) as well, and T_{bath} was measured at 433 mK. This gives Eq. 5.1, for the Aluminum phase separation model:

$$P = \frac{(T_{TES} - T_{bath})}{(R_{leg} + R_{unknown} * (Rn/R_{electrical}))} \tag{5.1}$$

Setting $(R_{unknown} * R_n)$ as one parameter and fitting the transition region with MCMC and optimal estimation techniques, we obtain the red fit in Fig. 5.5 to the blue data (with error bars). The fit gave $R_{leg} = 2.12874e{+}9[W/K] in [2.12867e{+}9, 2.12877e{+}9]$ with 0.68 confidence, and $R_{unknown} * R_n = 8.46910e+7[W^2/K^2] in [8.46743e+7, 8.46876e+7]$ with 0.68 confidence. This fit had a reduced Chi-squared of 9205.

Another possible refinement is considering the possibility of a two-stage temperature system, which was the source of the problem with the titanium but was not expected to be problematic at the aluminum TES's higher temperature. In this system, the island sits at a different temperature, T, from the bath or the TES. The island legs have a 3.5 exponent temperature dependence relation [1], resulting in this system of equations:

$$P = (\frac{R_{electrical}}{Rn}) * G_{TES-island} * (T_{critical} - T_{island}) \tag{5.2}$$

$$P = G_{island-bath} * (T^n_{island} - T^n_{bath}) \tag{5.3}$$

Where n is 3.5 for our legs. P must be the same by thermal equilibrium; if it was not, the appropriate places would very quickly heat and cool until it was, and the

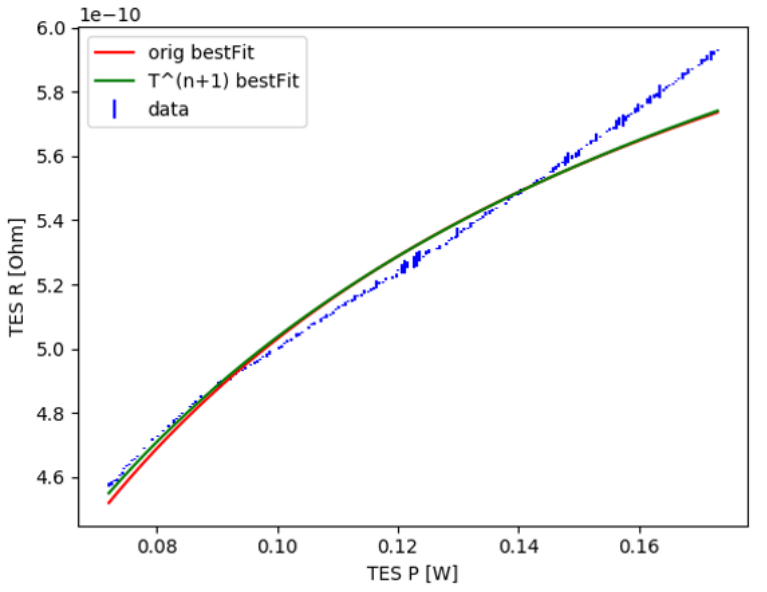

Figure 5.5: The two main models attempted, with fits given for a sample A-type detector.

same amount of heat power in total was flowing everywhere at any one time. These equations can be solved numerically (and for n= 3.5 must be solved numerically) for the island temperature, which can then be plugged in to model P.

The computational cost of getting the numerical roots was prohibitive for a million point MCMC run or even a 100,000 point run, which was typically the minimum needed for optimal capture. Thus we employed another common estimation and fit to the analytically solvable n=3 case instead. Results are given by the green fit in Fig. 5.5. $G_{TES-island}/R_n$ = 2.99890e-8 [W/(K Ohm)] in [2.99865e-8, 2.99923e-8] with 0.68 confidence. $G_{island-bath}$ = 2.21218e-10 [W/K] in [2.998654e-8, 2.999235e-8] w/ 0.68 confidence. Reduced Chi-squared of 8101.

A line on this data, in comparison, has a reduced Chi-squared of 708, suggesting that the model is deeply flawed. The line fit is given in Fig. **??**, and the line likelihood density and histogram of points are given in Figs. **??** and **??** as examples of the error computations performed and the checks for MCMC validity, which were done for all fits.

We also attempted to fit other detectors, A-type or not, and observed them to have roughly similar transition shapes and definitely similar quality of results. We tried including an additional sigma parameter for error; while this dramatically reduced the reduced Chi-squared, it had no significant effect on the calculated shape of the

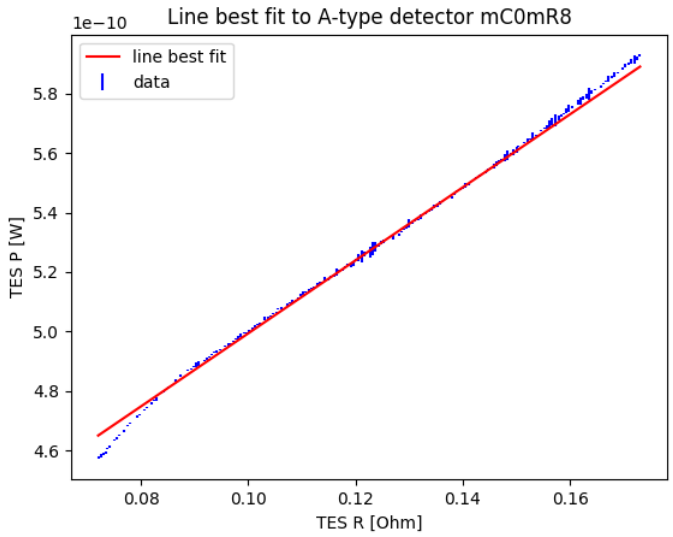

Figure 5.6: The best fit of a line to the A type detector, which had no currently known physical motivation.

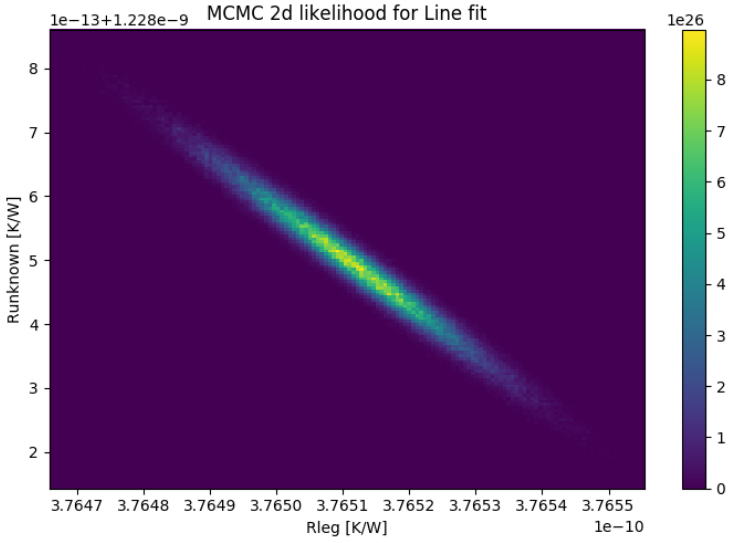

Figure 5.7: The 2d density plot of the best fit of a line to the A type detector. This is an important check on the validity of MCMC, as if multiple peaks had appeared more sophisticated techniques would have been necessary to accurately compare their height.

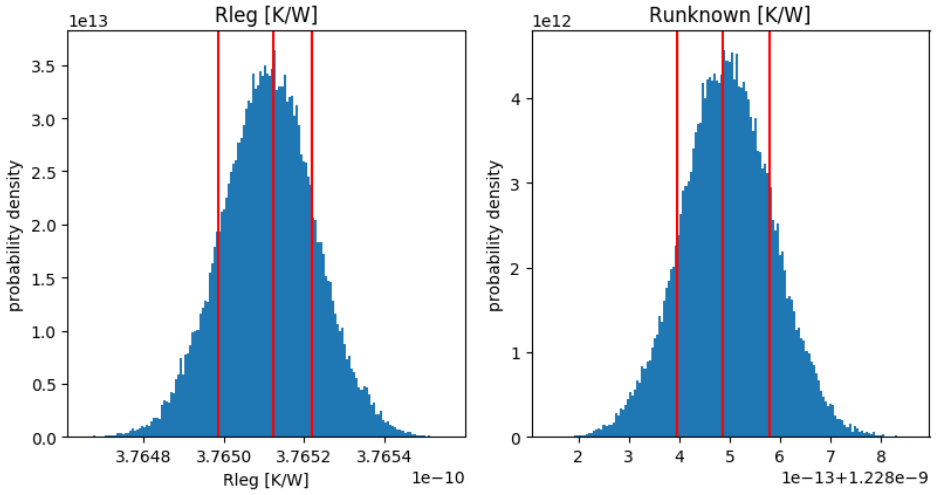

Figure 5.8: The histogram of MCMC point values of the best fit of a line to the A type detector. This is an important check on the validity of MCMC, which requires that parameters are roughly gaussian in likelihood distribution.

best fit line, which was still unquestionably off to the eye. We tried varying n in the two-stage model, in the range n = [0.5, 4]. 22 different 100,000+ step fits were performed and none of them looked remotely close. The line was the closest but unlike every other model attempted has no physical motivation and thus provides no useful information about device properties.

5.3 Superfast preliminary results

While superfast results have not yet been analyzed in depth, initial results were promising. The noise bump that was concerning in the original A-type detectors, illustrated in Fig. 5.9 appears greatly diminished in many (though not all) F (Fig. 5.10) and D (Fig. 5.11) type detectors.

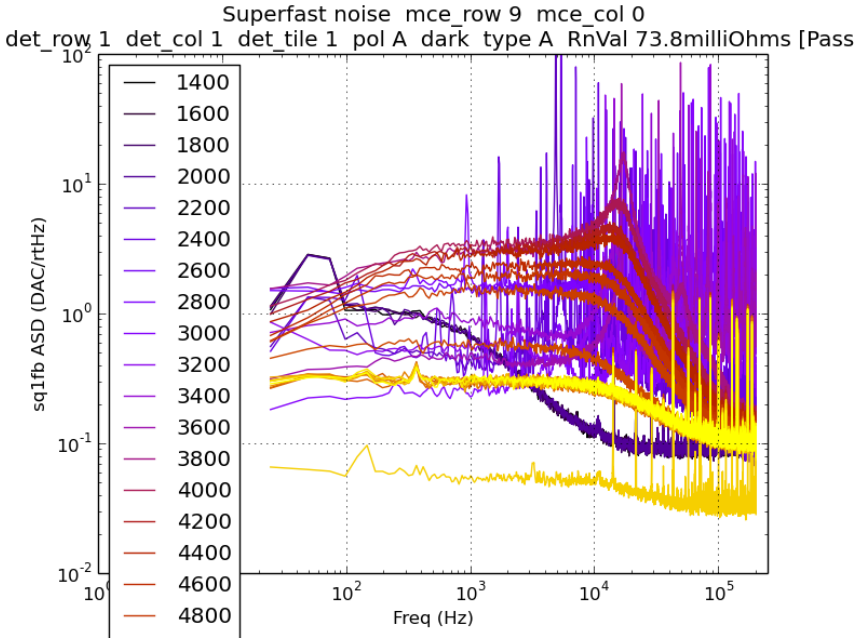

Figure 5.9: Fourier analysis of A-type detector for various current biases in DAC; amplitude vs. frequency. Note the "bump" of increase in frequency amplitude a bit bast 10^4.

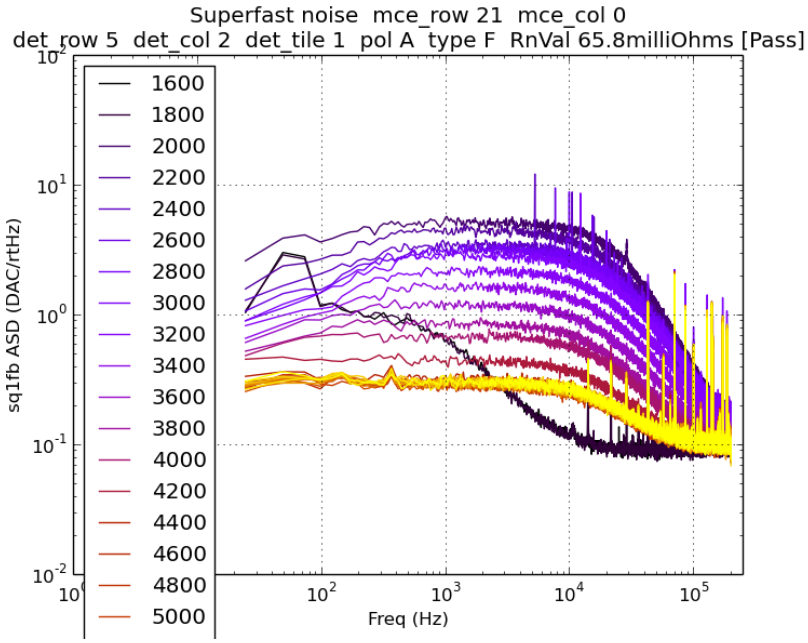

Figure 5.10: Fourier analysis of F-type detector for various current biases in DAC; amplitude vs. frequency. Note the lack of a "bump" of increase in frequency amplitude a bit bast 10^4.

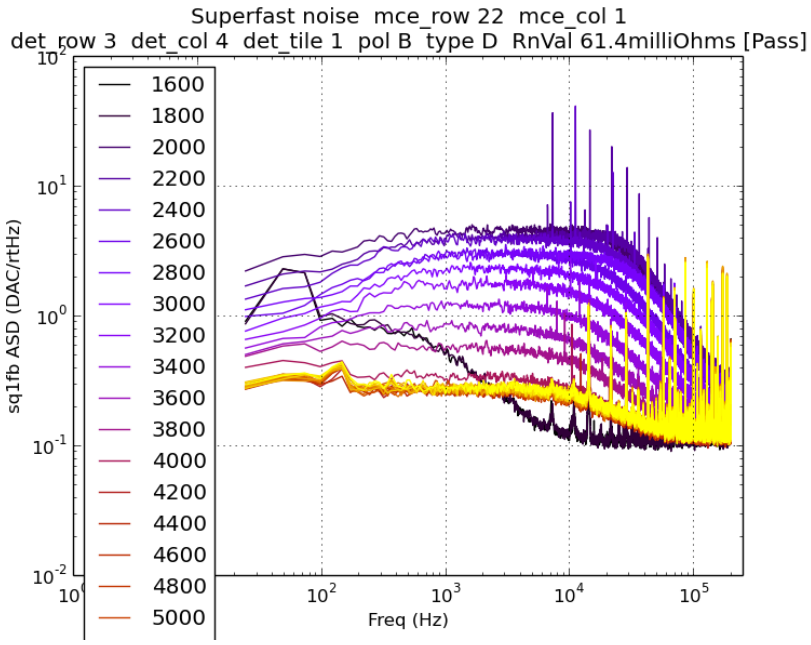

Figure 5.11: Fourier analysis of D-type detector for various current biases in DAC; amplitude vs. frequency. Note the lack of a "bump" of increase in frequency amplitude a bit bast 10^4.

5.4 Impedance

The admittance measurement was performed for detector types A,B,E and F. Representative plots of the admittance for an A and F type bolometer are shown in Fig. 5.12. For a detector in the transition, the admittance starts out negative real, then moves in a circle to positive imaginary and then positive real impedance. The histogram of fitted γ is shown in Fig. 5.13. The A-type measurements are consistent with the expected limiting thermal resistance calculated from Eq. 2.11, and the histogram indicates about a factor of three improvement in the internal thermal conductivity between the A and F type bolometers.

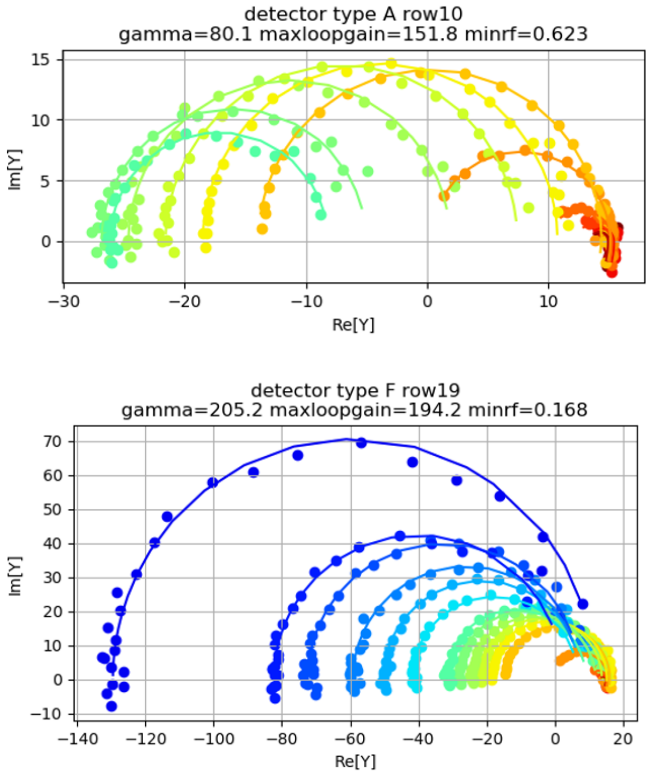

Figure 5.12: Fitted admittance for representative type A (top) and F (bottom) bolometers. Points are measured data, one point per frequency, lines are fits to the model. Color shows the bias voltage. Data is shown down to the lowest bias voltage where the detector remained stable.

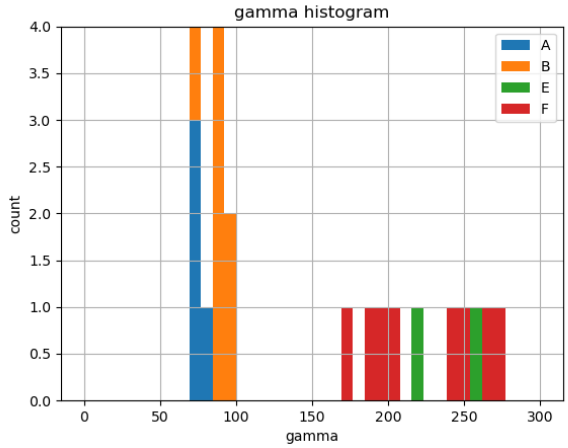

Figure 5.13: Histogram of fitted γ for the A,B,E and F detectors.

Chapter 6

CONCLUSIONS

The difficulty in operating our 270GHz detectors is consistent with low internal thermal conductivity in the bolometer, likely from the small cross-sectional area of the silicon nitride island.

Like George et al, despite the very different detector layout and different TES material (manganese doped aluminum), we find that the thermal conductivity could be increased by a factor of 2-3 by bringing the heat capacity metal closer to the TES film. The stabilized detectors better accommodate variations in optical load and detector properties, in principle allowing a multiplexed column of detectors to be operated at a single bias voltage with higher on sky yield.

While we have ruled out all cases in which phase-separation is the primary cause of the Aluminum's in-transition slope, and have similarly discarded the two-stage system as primarily relevant, the cause of the large slope in the Aluminum transition remains unclear. There are still a few unexplored possibilities. It is possible that TES temperature did vary significantly, that a nontrivial gradient exists between the two phase separated regions, that the TES critical temperature is current-dependent, and/or that Fourier's law is also incorrect for the mode of thermal transport in the normal region. While these effects were projected to be relatively small, further investigation into these possibilities will be taken.

In the future we plan to investigate whether the excess high frequency noise observed in Kernasovskiy et al[13] can be explained by the internal thermal resistance, and whether the modified detector types reduce the high frequency noise, potentially allowing for reduced sampling rates and higher multiplexing factors.

BIBLIOGRAPHY

[1] P. A. R. Ade and et. al. et. "Antenna-Coupled Bolometers used in BICEP2, KECK ARRAY, and SPIDER". In: *The Astrophysical Journal* (2015). URL: http://arxiv.org/pdf/1502.00619.pdf.

[2] AJ Anderson et al. "Modeling phase-separated transition-edge sensors in SuperCDMS detectors". In: *arXiv preprint arXiv:1109.3620* (2011).

[3] D. A. Bennett et al. "A Two-Fluid Model for the Transition Shape in Transition-Edge Sensors". In: *Journal of Low Temperature Physics* 167.3 (May 1, 2012), pp. 102–107. ISSN: 1573-7357. DOI: 10.1007/s10909-011-0431-4. URL: https://doi.org/10.1007/s10909-011-0431-4.

[4] Keck Array Collaboration BICEP and PAR Ade. "BICEP2/Keck Array VI: Improved Constraints On Cosmology and Foregrounds When Adding 95 GHz Data From Keck Array". In: *arXiv preprint arXiv:1510.09217* (2016).

[5] C. Eller. *Building BICEP2: A Conversation with Jamie Bock*. Web Page. 2014. URL: http://www.caltech.edu/news/building-bicep2-conversation-jamie-bock-42306.

[6] E. M. George and et al et. "A Study of Al-Mn Transition Edge Sensor Engineering for Stability". In: *Journal of Low Temperature Physics* 176.3 (2014). DOI: 10.1007/s10909-013-0994-3. URL: https://arxiv.org/abs/1311.2245.

[7] M. E. Gershenson et al. "Millisecond electron–phonon relaxation in ultrathin disordered metal films at millikelvin temperatures". In: *Applied Physics Letters* 79.13 (Sept. 2001), pp. 2049–2051. ISSN: 0003-6951, 1077-3118. DOI: 10.1063/1.1407302. URL: http://aip.scitation.org/doi/10.1063/1.1407302 (visited on 12/11/2017).

[8] J. M. Gildemeister. "Voltage-Biased Superconducting Bolometers for Infrared and mm-Waves". Ph.D. thesis. University of California, Berkely, 2000.

[9] W. Holmes et al. "Measurements of thermal transport in low stress silicon nitride films". In: *Appl. Phys. Lett.* 72.18 (Apr. 1998), pp. 2250–2252. ISSN: 0003-6951. DOI: 10.1063/1.121269. URL: http://aip.scitation.org/doi/10.1063/1.121269 (visited on 08/24/2017).

[10] W. Hu. *CMB Tutorial - Polarization - Gravitational Waves*. Web Page. 1996. URL: http://background.uchicago.edu/~whu/intermediate/Polarization/polar6.html.

[11] K. D. Irwin and G. C. Hilton. "Transition-Edge Sensors". In: *Cryogenic Particle Detection*. Topics in Applied Physics. DOI: 10.1007/10933596_3. Springer, Berlin, Heidelberg, July 2005, pp. 63–150. ISBN: 978-3-540-20113-

7 978-3-540-31478-3. URL: https://link.springer.com/chapter/10.1007/10933596_3 (visited on 10/04/2017).

[12] Keck Array and BICEP2 Collaborations. "Improved Constraints on Cosmology and Foregrounds from BICEP2 and Keck Array Cosmic Microwave Background Data with Inclusion of 95 GHz Band". In: *Phys. Rev. Lett.* 116.3 (Jan. 2016), p. 031302. DOI: 10.1103/PhysRevLett.116.031302. URL: https://link.aps.org/doi/10.1103/PhysRevLett.116.031302 (visited on 12/11/2017).

[13] S. Kernasovskiy et al. "Optimization and sensitivity of the Keck array". In: vol. 8452. International Society for Optics and Photonics, Sept. 2012, 84521B. DOI: 10.1117/12.926934. URL: https://www.spiedigitallibrary.org/conference-proceedings-of-spie/8452/84521B/Optimization-and-sensitivity-of-the-Keck-array/10.1117/12.926934.short (visited on 12/11/2017).

[14] Mark A. Lindeman et al. "Impedance measurements and modeling of a transition-edge-sensor calorimeter". In: *Review of Scientific Instruments* 75.5 (Apr. 2004), pp. 1283–1289. ISSN: 0034-6748. DOI: 10.1063/1.1711144. URL: http://aip.scitation.org/doi/abs/10.1063/1.1711144 (visited on 12/11/2017).

[15] Dan McCammon. "Thermal equilibrium calorimeters–an introduction". In: *Cryogenic particle detection*. Springer, 2005, pp. 1–34.

[16] Planck Collaboration. "Planck intermediate results. XXX. The angular power spectrum of polarized dust emission at intermediate and high Galactic latitudes". In: *Astronomy & Astrophysics* 586 (Feb. 2016). arXiv: 1409.5738, A133. ISSN: 0004-6361, 1432-0746. DOI: 10.1051/0004-6361/201425034. URL: http://arxiv.org/abs/1409.5738 (visited on 11/15/2017).

[17] P. L. Richards. "Bolometers for infrared and millimeter waves". In: *Journal of Applied Physics* 76.1 (1994), pp. 1–24. DOI: 10.1063/1.357128. URL: http://aip.scitation.org/doi/abs/10.1063/1.357128.

[18] P Santhanam and DE Prober. "Inelastic electron scattering mechanisms in clean aluminum films". In: *Physical Review B* 29.6 (1984), p. 3733.

[19] Jian Wei et al. "Ultrasensitive hot-electron nanobolometers for terahertz astrophysics". In: *Nat Nano* 3.8 (Aug. 2008), pp. 496–500. ISSN: 1748-3387. DOI: 10.1038/nnano.2008.173. (Visited on 08/24/2017).

[20] Adam L Woodcraft et al. "Thermal conductance measurements of a silicon nitride membrane at low temperatures". In: *Physica B: Condensed Matter* 284-288.Part 2 (July 2000), pp. 1968–1969. ISSN: 0921-4526. DOI: 10.1016/S0921-4526(99)02925-7. URL: http://www.sciencedirect.com/science/article/pii/S0921452699029257 (visited on 12/11/2017).

Appendix A

TITANIUM SAMPLE IV, PR AND TRANSITION-SELECT PLOTS FOR ALL TYPES

A.1 Characteristic IV plots

Fig.A.1 is typical of a functional type A, the original detector type. Observe how the instability, most prominent at low temperatures, shortens the available operating range of the detectors.

Fig.A.2 is typical of a functional type B detector, which added PdAu to the aluminum TES. It is quite similar to type A.

Fig.A.3 is typical of a functional type C detector, which had a PdAu finger and a via on the aluminum TES. While the instability is seemingly greatly diminished, the transition range still drops off at lower temperatures. The oddities in the superconducting region are due to a quirk of the readout electronics.

Fig.A.4 is typical of a functional type D detector, which had a PdAu finger on the titanium TES.

Fig.A.5 is typical of a functional type E detector, which had a PdAu finger and a via on the titanium TES. Note that many of the type E detectors failed the Rn cuts.

Fig.A.6 is typical of a functional type F detector, which coated the titanium and aluminum TES's in PdAu.

Fig.A.7 is typical of a functional type G detector, which coated the titanium and

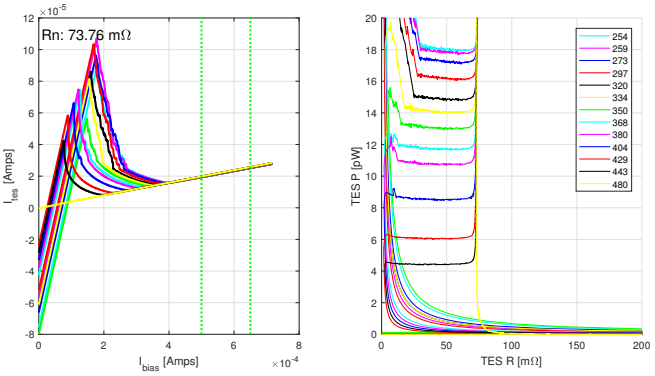

Figure A.1: Type A characteristic IV plot.

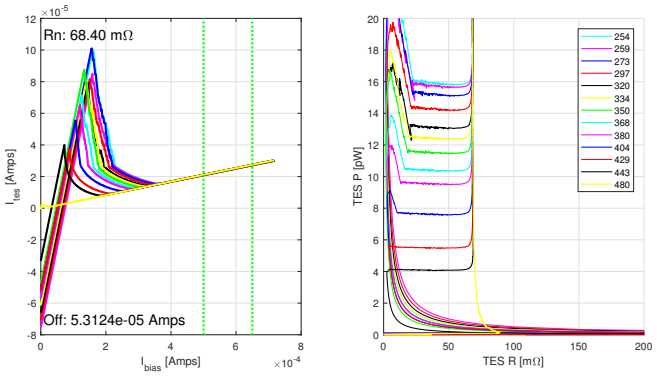

Figure A.2: Type B characteristic IV plot.

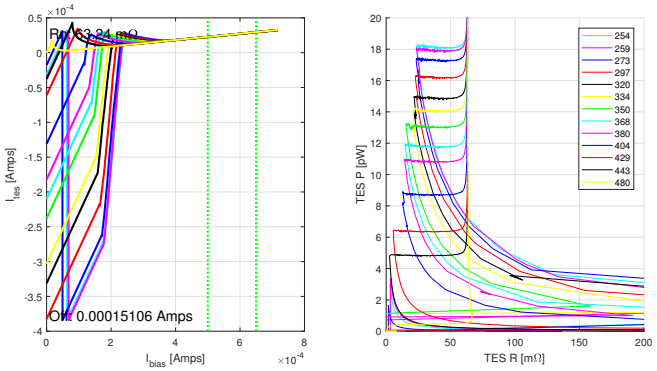

Figure A.3: Type C characteristic IV plot.

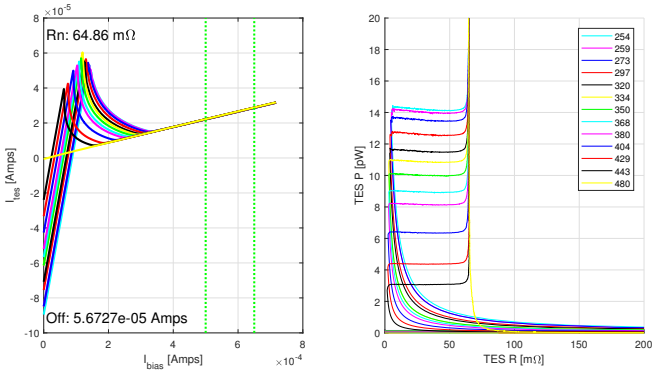

Figure A.4: Type D characteristic IV plot.

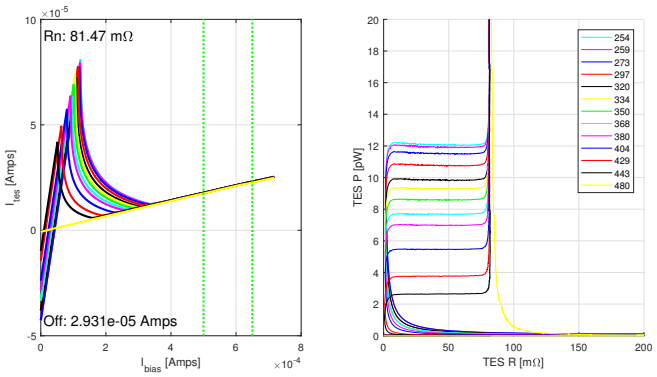

Figure A.5: Type E characteristic IV plot.

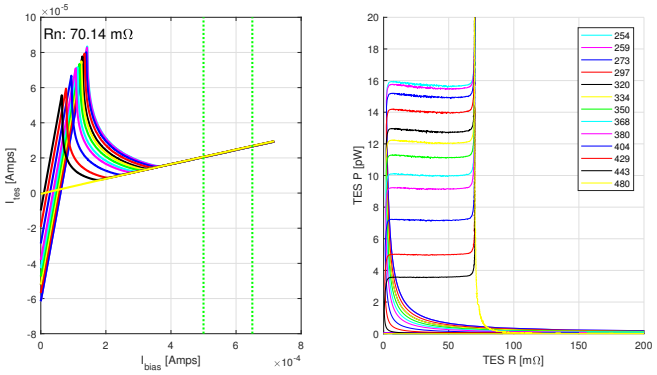

Figure A.6: Type F characteristic IV plot.

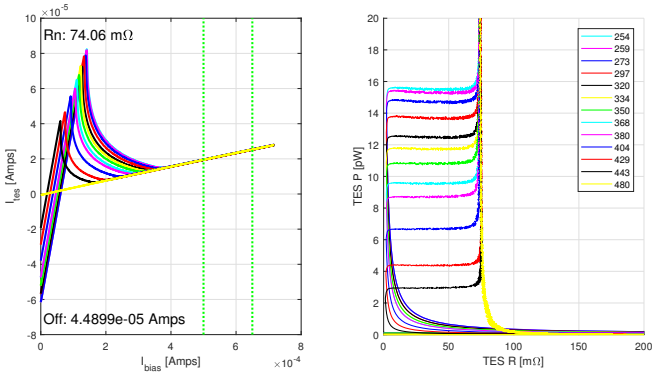

Figure A.7: Type G functional characteristic IV plot.

aluminum TES's in PdAu and had a via on the titanium TES. Note that many of the type G detectors failed the Rn cuts.

Fig.A.8 is typical of a functional type H detector, which had 3 vias on the aluminum TES, each coated with PdAu. It is very similar to type C.

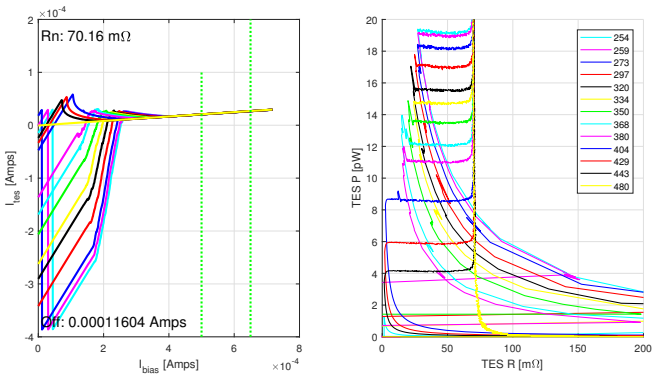

Figure A.8: Type H functional characteristic IV plot.

A.2 PR transition-select plots

Figures A.9, A.10, A.11, A.12, A.13, A.14, A.15, and A.16 illustrate the algorithm used to select the start and end of the usable transition range. The green lines mark the start (high end) of the transition range and the red lines mark the end (low end) of the transition range. They also display the pr plots for all functioning detectors of each type, for comparison. Note that some detectors did not have data taken due to failures of the readout system unrelated to the detectors, so simple number of plots is not equivalent to the detector yield.

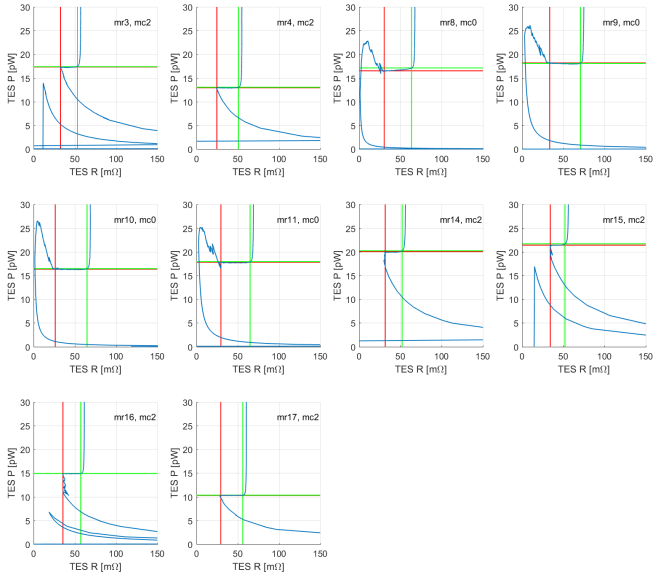

Figure A.9: Type A PR transition-select graph at 254mK.

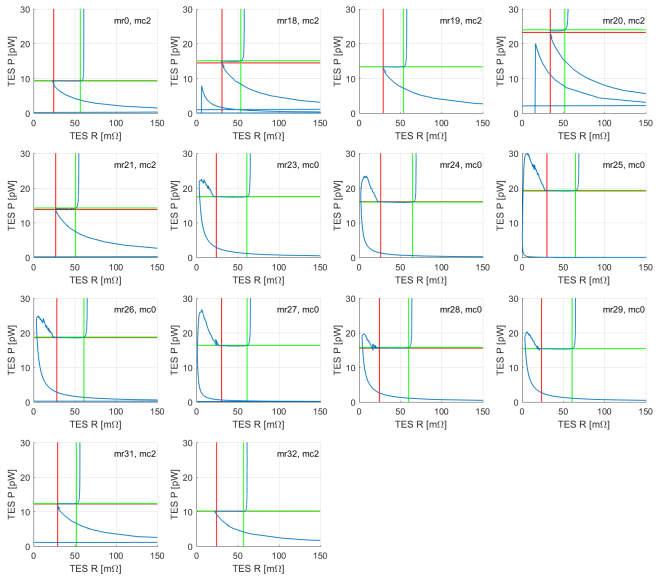

Figure A.10: Type B PR transition-select graph at 254mK.

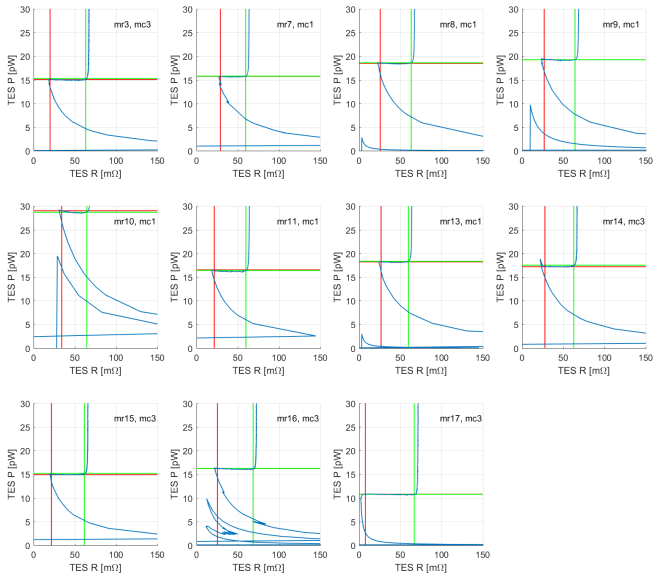

Figure A.11: Type C PR transition-select graph at 254mK.

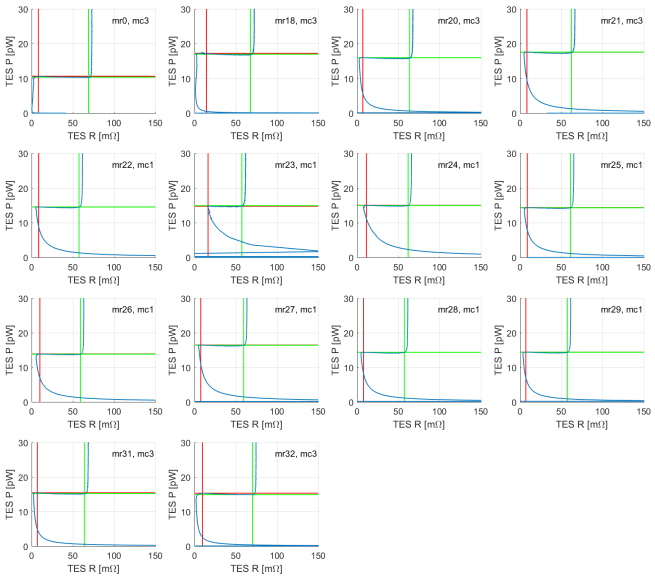

Figure A.12: Type D PR transition-select graph at 254mK.

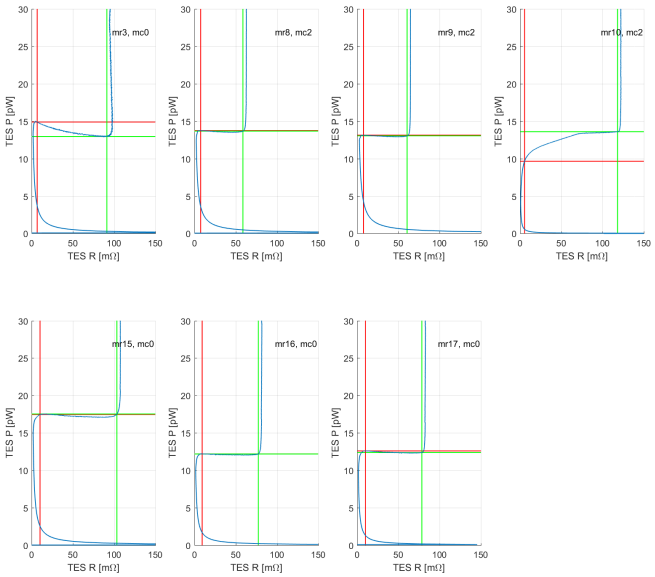

Figure A.13: Type E PR transition-select graph at 254mK.

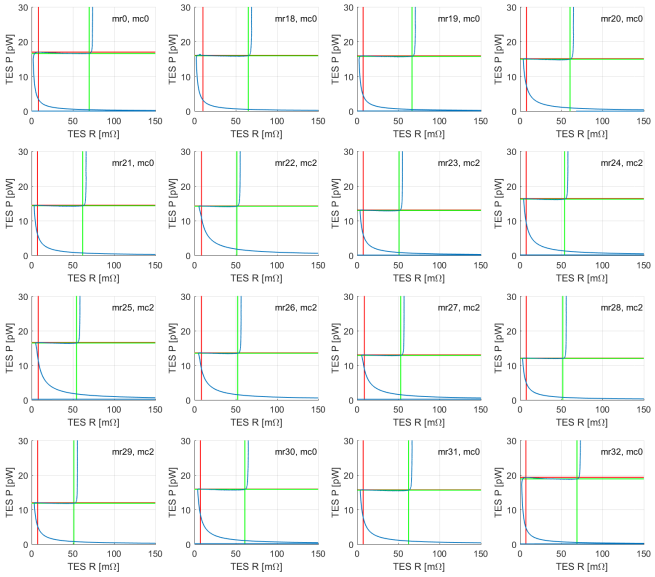

Figure A.14: Type F PR transition-select graph at 254mK.

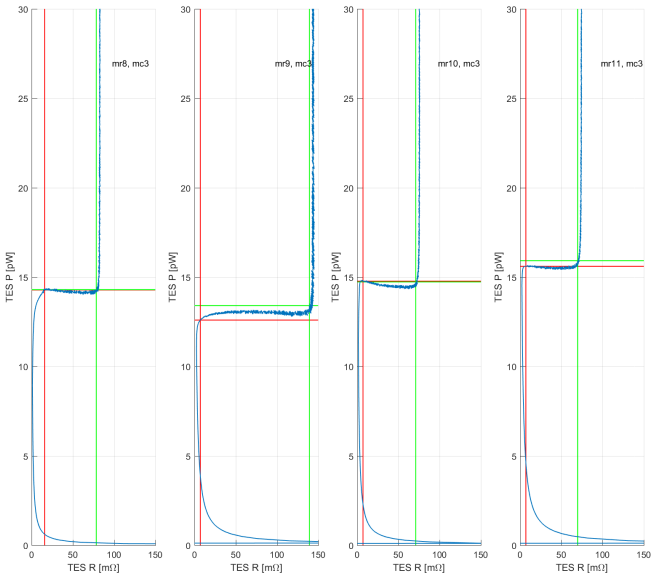

Figure A.15: Type G PR transition-select graph at 254mK.

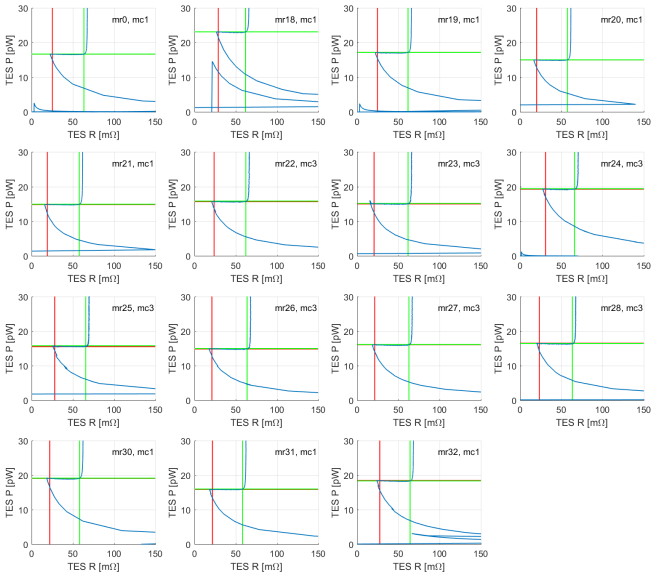

Figure A.16: Type H PR transition-select graph at 254mK.

A.3 Transition range graphs

Figures A.17, A.18, A.19, A.20, A.21, A.22, A.23, and A.24 display the critical metrics derived from the data. The first is detector yield, the percent of detectors of each type that displayed functional IV curves, not considering detectors where the readout system failed during tuning for reasons unrelated to the detectors.

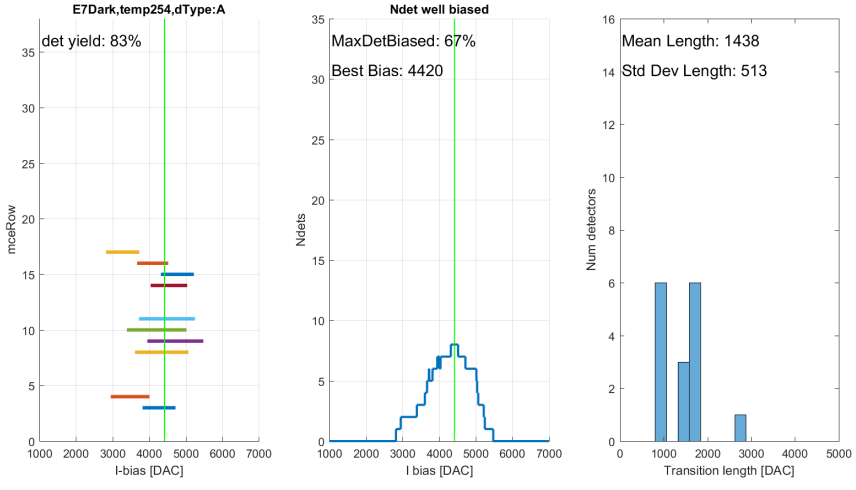

Figure A.17: Type A transition range graph at 254mK.

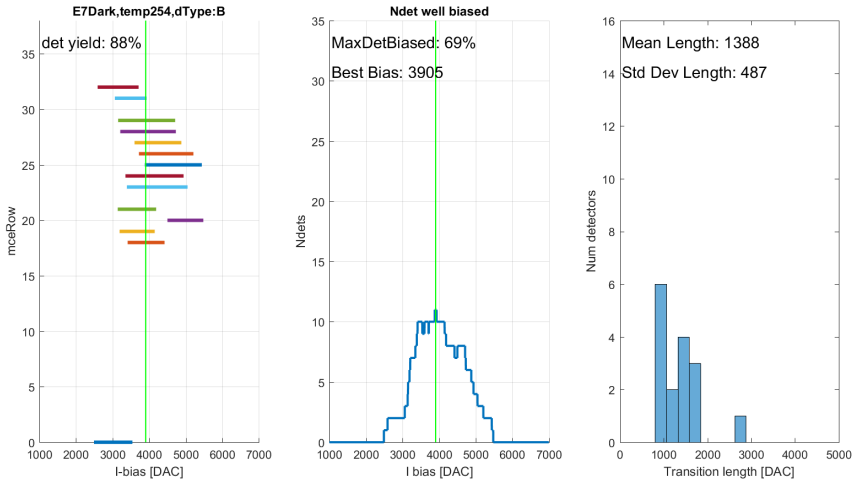

Figure A.18: Type B transition range graph at 254mK.

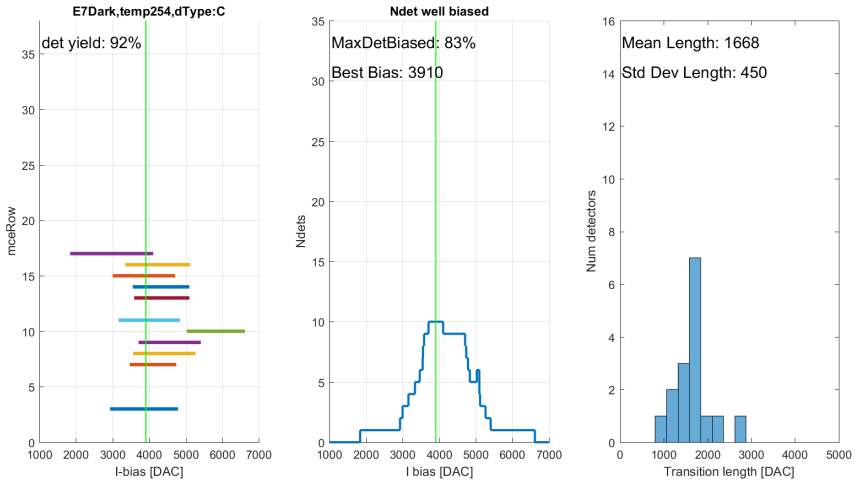

Figure A.19: Type C transition range graph at 254mK.

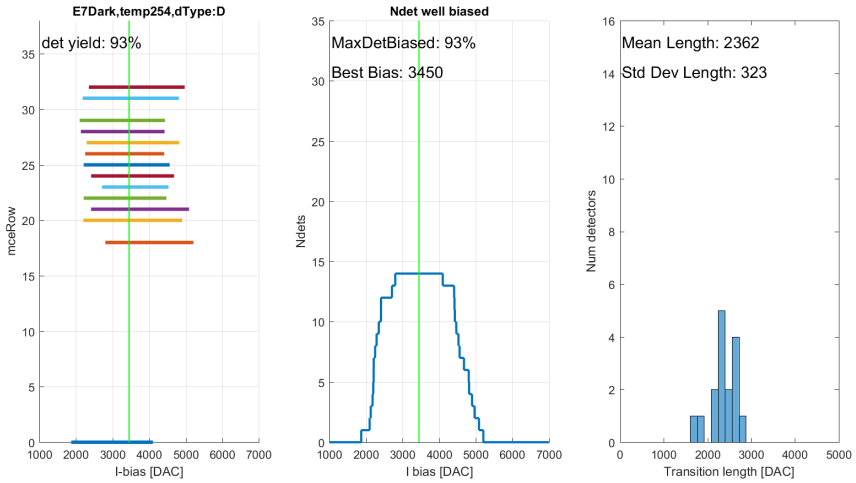

Figure A.20: Type D transition range graph at 254mK.

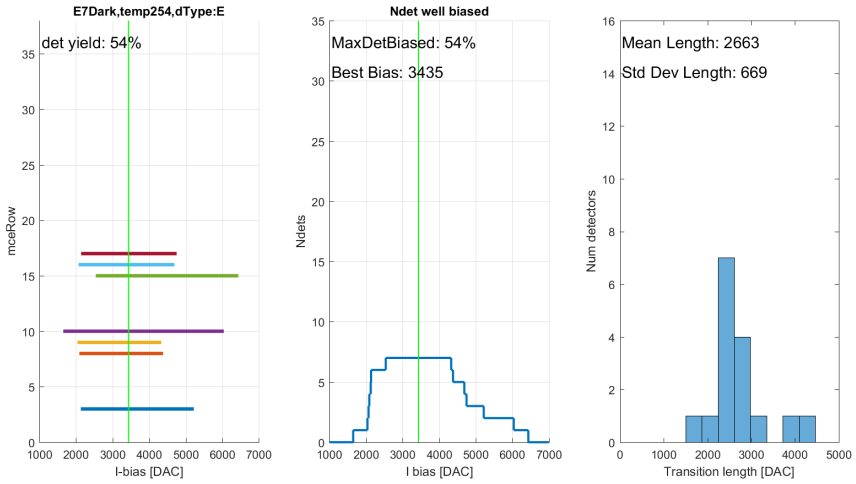

Figure A.21: Type E transition range graph at 254mK.

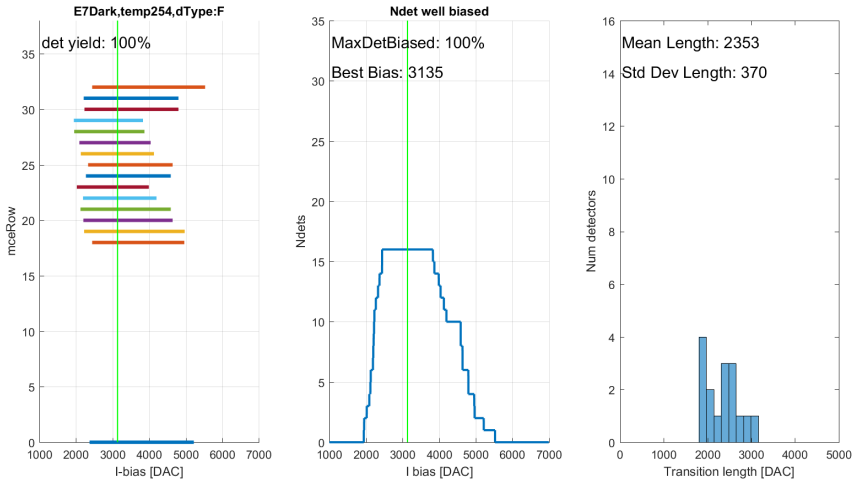

Figure A.22: Type F transition range graph at 254mK.

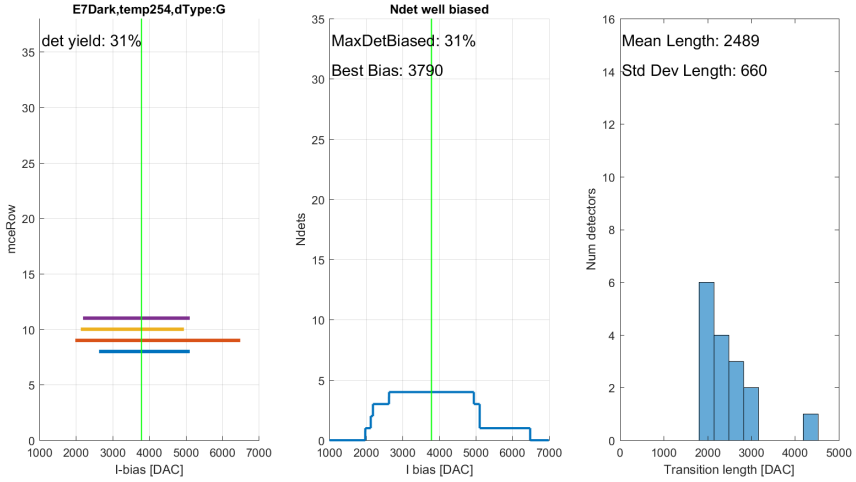

Figure A.23: Type G transition range graph at 254mK.

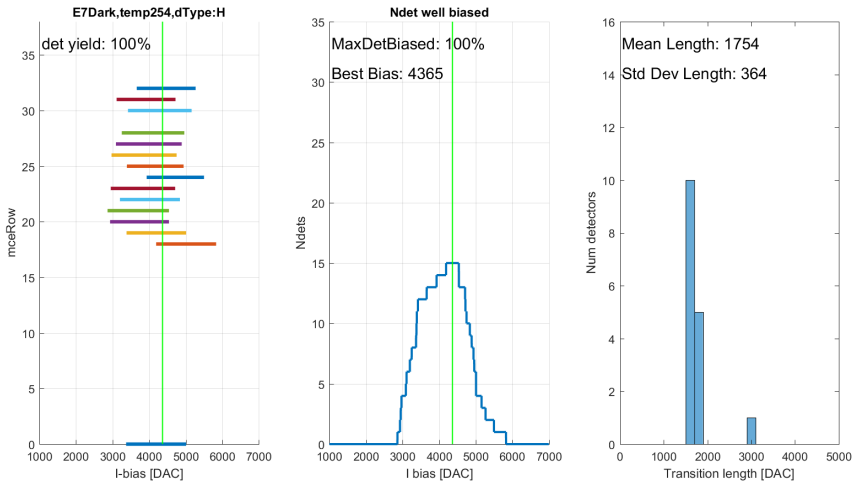

Figure A.24: Type H transition range graph at 254mK.